European Journal of Mechanics / A Solids 119 (2026) 106137

Contents lists available at ScienceDirect

European Journal of Mechanics / A Solids

journal homepage: www.elsevier.com/locate/ejmsol

Full length article

A gradient-damage model for amorphous glassy polymers: Consistent formulation of viscoplasticity and damage evolution in a micromorphic framework

Ayoub Hamdoun *, Rolf Mahnken, Richard Ostwald

Paderborn University, Warburger Straße 100, Paderborn, 33098, Germany

ARTICLE INFO

Keywords:
Glassy polymers
Gradient-enhanced damage
Viscoplasticity
Time-dependent damage
Regularization
Asymmetry

ABSTRACT

Polycarbonate (PC) is an amorphous polymer known for its advantageous mechanical properties, such as high tenacity and glass-like transparency. As a result, PC is widely used in various industries, including medical devices, the automotive sector, sporting equipment, and many other products. During its service life, PC undergoes plastic deformation, which leads to damage and eventual failure. Consequently, reliable material models are essential to predict such complex material behaviors and to reduce the need for costly experimental testing.

In this work, we develop a gradient-damage theory for amorphous glassy polymers within a micromorphic framework, accounting for both plastic deformation and damage. The evolution of damage is considered to have a temporal dependence, an aspect that has been underexplored, alongside the evolution of viscoplasticity. Both processes are consistently formulated in terms of free energy and potential functions. Arrhenius-type multipliers are employed to describe the evolution of plasticity and damage. This theory is implemented within a finite element framework, and several numerical examples, including both homogeneous and inhomogeneous cases, are presented to demonstrate its capabilities.

1. Introduction

Polycarbonate (PC) is widely used in industrial applications due to its favorable mechanical properties, such as high strength and good processability. Nevertheless, its mechanical performance is often limited by damage mechanisms including crazing, shear yielding, and microcracking, which initiate and evolve under complex loading conditions. Accurate prediction of the mechanical response and failure of such materials therefore requires constitutive frameworks capable of capturing the coupled evolution of viscoplastic deformation and damage.

The development of constitutive and damage models for glassy polymers has progressed significantly over the past decades. Early micromechanical insights were provided by Argon (1973), who highlighted the role of localized shear transformations in plastic deformation. Building on this foundation, Boyce et al. (1988) proposed a constitutive model incorporating both viscoelastic and viscoplastic responses, which has become a benchmark for describing large-strain polymer behavior. Subsequently, Anand and Gurtin (2003) introduced a thermodynamically consistent framework to model the interaction between viscoplasticity and damage, while Estevez and Van der Giessen (2005) emphasized the importance of coupling mechanical and environmental effects in damage modeling. In Zaïri et al. (2008), constitutive equations based on a modified Bodner–Partom model were proposed to describe elasto-viscoplastic damage in rubber-toughened glassy polymers, incorporating hydrostatic stress and void evolution with strong agreement to experimental data. A thermodynamically based constitutive model for thermoplastic polymers was further developed in Krairi and Doghri (2014), where total strain is decomposed into viscoelastic and viscoplastic components, and ductile damage evolution is linked to viscoplastic strains with isotropic and nonlinear kinematic hardening.

Beyond constitutive modeling, the rate dependence of damage evolution represents a critical but comparatively less explored aspect of continuum damage mechanics. In Lemaitre (1985), the dissipation potential is decomposed into viscoplastic and damage-related contributions, both formulated as time-dependent processes. More recently, Lamm et al. (2024a) derived evolution multipliers from plastic and damage potentials with temporal dependence expressed through Perzyna-type formulations, highlighting the importance of rate effects in coupled damage–plasticity processes.

* Corresponding author.
E-mail addresses: ayoub.hamdoun@uni-paderborn.de (A. Hamdoun), mahnken@ltm.upb.de (R. Mahnken), richard.ostwald@uni-paderborn.de (R. Ostwald).

https://doi.org/10.1016/j.euromechsol.2026.106137
Received 6 December 2025; Received in revised form 30 March 2026; Accepted 1 April 2026
Available online 16 April 2026

A further key challenge in modeling glassy polymers is the pronounced asymmetry between tensile and compressive behavior. While these materials tend to fail under tension, they can sustain significant plastic deformation under compression, a behavior largely attributed to crazing and microvoid growth under tensile stress. Several modeling approaches have been proposed to represent this asymmetry. Phase-field models, such as that in Yin and Kaliske (2020), consider degradation of only the fracture-driving part of the energy function, whereas the framework proposed in Mahnken (2003), Shaban et al. (2007) and Mahnken et al. (2008) introduces stress-mode-dependent weighting functions in flow rules, damage evolution, and material parameters. By assigning separate weighting functions to tensile, compressive, and shear stress modes, such approaches capture the softer tensile response and the more resistant compressive behavior observed in polymers and other engineering materials.

However, local damage formulations often suffer from pathological mesh dependence associated with strain softening and damage localization. To address this limitation, nonlocal and gradient-based regularization techniques have been extensively developed. Integral-type nonlocal models represent one of the earliest strategies, in which state variables are spatially averaged over a characteristic interaction length to regularize localization (Peerlings et al., 2001), although their application is often limited by computational cost and implementation complexity. Gradient-enhanced damage and plasticity models provide an alternative by introducing internal length scales through higher-order spatial gradients of damage or plastic strain. The theoretical foundations of gradient damage were initially developed for quasi-brittle materials and later extended to ductile fracture and finite-strain formulations (Peerlings et al., 1996; Comi, 2001; Engelen et al., 2006). These approaches were subsequently generalized to coupled damage–plasticity mechanisms, enabling objective simulation of strain localization and post-peak softening (de Borst and Pamin, 1996; Geers et al., 1998).

Micromorphic formulations enable a mathematically consistent framework for gradient-enhanced damage by introducing additional kinematic fields and balance equations, with applications to ductile damage and gradient plasticity at finite strains (Forest, 1998, 2009; Forest et al., 2011) and further conceptual extensions coupling gradient-enhanced plasticity with ductile damage and viscoplasticity (Brepols et al., 2017a). For amorphous glassy polymers applications, nonlocal and gradient-enhanced theories introduce intrinsic length scales, enabling mesh-objective simulations of post-yield softening and ultimate failure (Nguyen et al., 2014, 2016; Narayan and Anand, 2021). Other gradient formulations have been developed for semicrystalline polymers, where damage is coupled with rate-dependent viscoplasticity at large strains (Wiersma and Sain, 2023; Satouri et al., 2022, 2025; Lamm et al., 2024b).

Beyond classical damage descriptions, theories including viscodamage have been introduced to capture rate dependency under complex loading conditions (Voyiadjis et al., 2012). Recent constitutive models of amorphous glassy polymers combine viscoelasticity with viscoplastic flow, enabling accurate predictions over wide ranges of strain rate and temperature (Alves et al., 2023; Ferreira et al., 2023; Zhou et al., 2023). These models provide a robust and thermodynamically consistent basis for large-deformation simulations and natural coupling with gradient-enhanced damage and fracture formulations.

Multiscale methods have been employed to investigate fracture mechanisms in glassy polymers, linking molecular-scale deformation processes, craze evolution, and macroscopic fracture resistance (Zhao et al., 2024a,b; Laschütza and Seelig, 2025). These studies underscore the critical role of microstructural mechanisms in crack initiation, cyclic craze growth, and failure under complex loading histories.

Recent gradient- and micromorphic-enhanced formulations have been proposed to regularize localization in coupled plasticity–damage models formulated in logarithmic strain space. Friedlein et al. (2023) developed and compared different gradient-enhancement strategies for plasticity–damage coupling, focusing on the comparison between additive and multiplicative strain decompositions. Their formulation employs a comparatively simple damage evolution law and does not explicitly account for a distinct damage yield surface or damage-driven threshold mechanisms. The authors in Brepols et al. (2017b), Holthusen et al. (2022) and Lamm et al. (2024b) proposed a gradient-enhanced plasticity–damage model based on a double-surface concept, in which separate yield surfaces govern plasticity and damage evolution. Their model incorporates time-dependent damage evolution and explicitly accounts for a damage activation criterion, leading to improved numerical robustness and mesh-objective responses in finite strain simulations. However, despite these advances, existing models do not fully capture the thermally activated rate dependence of damage and the pronounced tension–compression asymmetry characteristic of glassy polymers.

In this work, we propose a gradient-enhanced viscoplastic damage model tailored to glassy polymers, combining a novel damage–plasticity formulation with micromorphic regularization. Building on the Lemaitre damage framework, the model provides a physically consistent description of the coupled evolution of plasticity and damage, both treated as time-dependent processes, an interaction that remains relatively underexplored. Plastic and damage potentials are introduced in a unified manner, enabling a consistent derivation of the associated evolution equations. Both processes are formulated with Arrhenius-type multipliers and are thermally activated. The unified hardening laws govern damage and plasticity, derived directly from energy function.

Our model is implemented using an eight-node nonlinear brick element with four degrees of freedom at each node. In the first stage, we demonstrate the homogeneous material response through a single-element test to highlight the key characteristics of the model. The numerical analysis performed on various specimens shows that the model effectively addresses the issue of shear band localization and provides a plausible prediction of the crack path.

The structure of the paper is as follows: Section 2 introduces the thermodynamic framework underlying the micromorphic model, and presents a general formulation for viscoplasticity coupled with time-dependent damage. Section 3 addresses the numerical aspects, including the integration scheme and the computation of algorithmic tangent moduli. Section 4 demonstrates the application of the proposed theory through numerical analyses of a one-element test and various specimen geometries. Finally, Section 5 offers concluding remarks and discusses directions for future research.

Notations

Square brackets $[\bullet]$ denote 'function of' and are used to distinguish this from mathematical groupings with parentheses $(\bullet)$.

2. Constitutive modeling for gradient enhanced damage model within micromorphic framework

2.1. Kinematics

Infinitesimal line elements $\mathrm{d}\mathbf{X}$ in the reference configuration $\mathscr{B}_0$ at $t = 0$ are mapped to $\mathrm{d}\mathbf{x}$ in the current configuration $\mathscr{B}_t$ by the deformation gradient $\mathbf{F}$. We define the Jacobian $J = \det \mathbf{F}$, which quantifies the local volume change and maps a reference volume element $\mathrm{d}V$ in $\mathscr{B}_0$ to the current element $\mathrm{d}v$ in $\mathscr{B}_t$ via $\mathrm{d}v = J\,\mathrm{d}V$.

$$1.\ \mathrm{d}\mathbf{x} = \mathbf{F}\,\mathrm{d}\mathbf{X}, \qquad 2.\ \mathrm{d}v = J\,\mathrm{d}V, \tag{1}$$

and the gradient $\boldsymbol{H}$ of the micromorphic variable ϕ is defined as

$$\mathrm{d}\phi = \boldsymbol{H} \cdot \mathrm{d}\mathbf{X}. \tag{2}$$

In this paper, we develop a finite-plasticity framework expressed in terms of the total Hencky strain tensor $\mathbf{E}$ in logarithmic form; see Hencky (1928), Seth (1964), Ogden (1984) and Silhavy (1997). We treat this strain measure as a function of the right Cauchy–Green tensor $\mathbf{C}$, namely:

$$1.\ \mathbf{C} = \mathbf{F}^t \cdot \mathbf{F}, \qquad 2.\ \mathbf{E} = \frac{1}{2}\ln \mathbf{C}. \tag{3}$$

For the subsequent analysis, two fourth-order projection tensors and a material rate-of-deformation tensor are introduced:

$$1.\ \mathbb{I}^{dev} = \mathbb{I} - \frac{1}{3}\mathbf{1}\otimes\mathbf{1}, \qquad 2.\ \mathbb{P} = 2\frac{\partial \mathbf{E}}{\partial \mathbf{C}}, \qquad 3.\ \mathbf{D}[t] = \frac{1}{2}\dot{\mathbf{C}}[t], \tag{4}$$

where $\mathbf{1}$ and $\mathbb{I}$ are second- and fourth-order unit tensors, respectively, and where the dot above the argument denotes the derivative with respect to time t. Furthermore, by use of the spectral decomposition,

$$1.\ \mathbf{C} = \sum_{A=1}^{3} \lambda_A^2 \mathbf{M}^A \quad \Longrightarrow \quad 2.\ \mathbf{E} = \frac{1}{2}\sum_{A=1}^{3} \ln \lambda_A^2 \mathbf{M}^A, \tag{5}$$

the following relation can be shown:

$$\ln J = \frac{1}{2} 2 \ln\det \mathbf{F} = \frac{1}{2}\ln\det \mathbf{C} = \frac{1}{2}\ln[\lambda_1^2\lambda_2^2\lambda_3^2] = \frac{1}{2}\sum_{A=1}^{3}\ln\lambda_A^2 = \mathrm{tr}\mathbf{E}. \tag{6}$$

The total Hencky-strain tensor is additively decomposed into elasto- and viscoplastic parts as

$$\mathbf{E} = \mathbf{E}^p + \mathbf{E}^e. \tag{7}$$

2.2. Constitutive relations

Following the approach in Forest (2009), we introduce the linear momentum and micro balance together with the entropy and energy equations

$$\begin{array}{llcll}
1. & \ddot{\mathbf{u}} - \mathrm{Div}[\mathbf{F}\cdot\mathbf{S}] & = & \mathbf{b} & \text{(linear momentum)} \\
2. & \rho_0\,\dot{e} + \mathrm{Div}\,\mathbf{q}_0 & = & \mathcal{P} + \rho_0\, r_\theta & \text{(energy)} \\
3. & -\rho_0\,\dot{e} + \rho_0\,\theta\,\dot{\eta} + \mathcal{P} - \dfrac{1}{\theta}\,\mathbf{q}_0\cdot\mathrm{Grad}\,\theta & \geq 0 & & \text{(entropy)} \\
4. & \hat{a} - \mathrm{Div}\,\boldsymbol{\zeta} & = & m & \text{(micro balance)}
\end{array} \tag{8}$$

and where

$$\mathcal{P} = \mathbf{S} : \mathbf{D} + \boldsymbol{\zeta}\cdot\dot{\boldsymbol{H}} + \hat{a}\dot{\phi} \tag{9}$$

is the *mechanical power* due to macroscopic and micromorphic variable related stresses and forces, Forest (2009). In accordance with and in addition to the previous notations we use: ρ_0 - density in the reference configuration, $\mathbf{u}$ - displacement vector, $\mathbf{D}$ - material rate of deformation tensor of Eq. ((4).3), θ - absolute temperature, $\mathbf{S}$ - (symmetric) 2nd Piola–Kirchhoff stress tensor, $\mathbf{b}$ - mass density of external forces, e - mass density of the internal energy, $\mathbf{q}_0$ - heat-flux density vector, η - entropy per unit mass, r_θ - mass density of heat supply, $\dot{\boldsymbol{H}}$ - rate of microstrain, $\boldsymbol{\zeta}$ - damage microstress, $\hat{a}$ - damage microforce, m - damage micro load, and where the terminology "micro" is a synonym for micromorphic variable related quantities. We also recall, that the inequality ((8).3) is known as the *Clausius–Duhem inequality*.

Upon using a Legendre-transformation between the internal energy e and the Helmholtz energy Ψ via relation $\Psi = e - \theta\,\eta$, the inequality ((8).3) becomes

$$\begin{array}{llcl}
1. & \mathcal{D} & = & \mathcal{D}^{\mathrm{me}} + \mathcal{D}^{\mathrm{th}} \geq 0, \text{ where} \\
2. & \mathcal{D}^{\mathrm{me}} & = & \mathcal{P} - \rho_0\dot{\Psi}, \\
3. & \mathcal{D}^{\mathrm{th}} & = & -\rho_0\dot{\theta}\eta - \dfrac{1}{\theta}\mathbf{q}_0\cdot\mathrm{Grad}\,\theta.
\end{array} \tag{10}$$

Here $\mathcal{D}^{\mathrm{me}}$ and $\mathcal{D}^{\mathrm{th}}$ are mechanical and thermal dissipation terms, respectively. In the sequel, we restrict ourselves to the mechanical part subjected to isothermal conditions and require

$$\mathcal{D}^{\mathrm{me}} = \mathcal{P} - \rho_0\dot{\Psi} = \mathbf{S} : \mathbf{D} + \boldsymbol{\zeta}\cdot\dot{\boldsymbol{H}} + \hat{a}\ \dot{\phi} - \rho_0\dot{\Psi} \geq 0, \tag{11}$$

which means the temperature is maintained constant over time during loading, while the material response remains temperature-dependent. Let us assume the functional relationship

$$\Psi = \Psi[\mathbf{E}^e, {}^p\underline{q}, \boldsymbol{H}, d, \phi, {}^d\underline{q}] \tag{12}$$

for the Helmholtz energy, where $\mathbf{E}^e$ is the elastic part of the Hencky strain tensor in Eq. (7) and ${}^p\underline{q} = ({}^pq_1, \ldots, {}^pq_n)$ is a vector of ${}^pn$ hardening internal variables of strain type. Analogously, we introduce ${}^d\underline{q} = ({}^dq_1, \ldots, {}^dq_n)$ as a vector of ${}^dn$ of damage hardening internal variable of strain type. d and ϕ are isotropic damage and micromorphic damage variables, respectively.

Next, by use of the kinematic decomposition Eq. (7) the time derivative of the Helmholtz energy Ψ multiplied by the (bulk) density ρ_0 is obtained from Eq. (12) as

$$\begin{array}{rcl}
\rho_0\dot{\Psi} & = & \rho_0\dfrac{\partial\Psi}{\partial\mathbf{E}^e} : (\dot{\mathbf{E}} - \dot{\mathbf{E}}^p) + \rho_0\dfrac{\partial\Psi}{\partial\,{}^p\underline{q}}\cdot{}^p\underline{\dot{q}} + \rho_0\dfrac{\partial\Psi}{\partial d}\dot{d} + \rho_0\dfrac{\partial\Psi}{\partial\boldsymbol{H}}\cdot\dot{\boldsymbol{H}} + \rho_0\dfrac{\partial\Psi}{\partial\phi}\dot{\phi} + \rho_0\dfrac{\partial\Psi}{\partial\,{}^d\underline{q}}\,{}^d\underline{\dot{q}} \\
& = & \mathbf{T} : \mathbb{P} : \mathbf{D} - \mathbf{T} : \dot{\mathbf{E}}^p + {}^p\underline{Q}\cdot{}^p\underline{\dot{q}} + Y_d\dot{d} + \boldsymbol{\zeta}\cdot\dot{\boldsymbol{H}} + \hat{a}\dot{\phi} + {}^d\underline{Q}\,{}^d\underline{\dot{q}},
\end{array} \tag{13}$$

where $\mathbb{P}$ and $\mathbf{D}$ are defined in Eqs. ((4).2) and ((4).3), respectively.

In the sequel, we provide a concrete formulation of the Helmholtz energy function in Eq. (12), which is split into a local part Ψ^{loc} and nonlocal part Ψ^{nloc} as

$$
\begin{aligned}
&1.\quad \Psi[\mathbf{E}^e, {}^p\underline{q}, \boldsymbol{H}, \phi, d] = \Psi^{loc}[\mathbf{E}^e, {}^p\underline{q}, d, \phi] + \Psi^{nloc}[\boldsymbol{H}, \phi, d], \quad \text{where}\\
&2.\quad \Psi^{loc} = \Psi^{iso} + \Psi^{vol} + \Psi^{p}\\
&3.\quad \Psi^{iso} = f_{dev}(d)\frac{G}{\rho_0}\mathbf{E}^e_{dev} : \mathbf{E}^e_{dev},\\
&4.\quad \Psi^{vol} = f_{vol}(d)\frac{K}{2\rho_0}\left(\mathrm{tr}\left[\mathbf{E}^e\right]\right)^2,\\
&5.\quad \Psi^{p} = \sum_{i=1}^{n=2}\frac{1}{2\rho_0}H_i\,{}^pq_i^2,\\
&6.\quad \Psi^{nloc} = \frac{1}{2\rho_0}{}^{\chi}H(\phi-d)^2 + \frac{{}^{\chi}A}{2\rho_0}\boldsymbol{H}\cdot\boldsymbol{H} + \sum_{i=1}^{n=2}\frac{1}{2\rho_0}H_{di}\,{}^dq_i^2.
\end{aligned}
\tag{14}
$$

The terms Ψ^{iso} and Ψ^{vol} take storage quantities related to the elastic strains $\mathbf{E}^e$ into account. The first term considers isochoric elastic deformations, where $\mathbf{E}^e_{dev} = \mathbb{I}^{dev} : \mathbf{E}^e = \mathbf{E}^e - \mathrm{tr}[\mathbf{E}^e]\mathbf{1}/3$ and $\mathbf{1}$ is the second order unit tensor. The second term considers volumetric elastic deformations. For an isotropic material G and K are the shear modulus and the bulk modulus respectively. The inelastic part Ψ^p of the Helmholtz energy is defined in Eq. ((14).4). It accounts for energy storage due to inelastic deformations, more concretely to combined linear and nonlinear isotropic hardening. ${}^pq_1$ and ${}^pq_2$ are (scalar) internal variables of strain type, such that its number is ${}^pn = 2$. H_i, $i = 1, 2$ are material parameters. The nonlocal part Ψ^{nloc} of the Helmholtz energy is defined in Eq. ((14).6). It accounts for energy storage due to microstructural properties consisting of two scalar type parts and a gradient type part. ${}^{\chi}H$ is a damage coupling modulus that forces proximity between the macro and micro variables ϕ and d, ensuring a regularization effect and ${}^{\chi}A$ is a damage regularization parameter. The last term of the nonlocal part of the energy function accounts for the energy storage due to damage evolution, where ${}^dq_1$ and ${}^dq_2$ are damage hardening variables, such its number is ${}^dn = 2$. $H_{di}, i = 1, 2$ are material parameters.

In this work, the damage function is decomposed into deviatoric and volumetric contributions to distinguish between shear-driven and dilatational degradation mechanisms, as introduced in the original work of Kiefer et al. (2018), Sprave and Menzel (2020) and Schulte et al. (2020). Particular focus is placed on the deviatoric damage component, which is assigned greater weight in the overall damage evolution, as demonstrated later in our numerical analysis. This modeling choice is physically motivated by the fact that amorphous glassy polymers typically exhibit nearly incompressible behavior under mechanical loading, as confirmed by our experimental investigation on glassy polymers in Hamdoun and Mahnken (2024b). In such materials, the volumetric stress state contributes only marginally to material degradation. Damage processes such as void nucleation and growth are relatively limited compared to deviatoric mechanisms — such as shear yielding and crazing — which dominate the material response. These phenomena are inherently deviatoric in nature and are directly linked to significant stiffness degradation and failure. Therefore, treating the volumetric and deviatoric components of damage separately allows our model to more accurately capture the experimentally observed mechanical behavior.

We define the volumetric, deviatoric degradation functions f_{vol}, f_{dev} in Eq. (14) as

$$
\begin{aligned}
&1.\quad f_{vol}(d) = \exp(-\eta_{vol}d),\\
&2.\quad f_{dev}(d) = \exp(-\eta_{dev}d),
\end{aligned}
\tag{15}
$$

where η_{vol} and η_{dev} are the volumetric and deviatoric saturation parameters.

With the Helmholtz energy in the Eq. (14), the thermodynamic forces are obtained as

$$
\begin{aligned}
&1.\quad \mathbf{T} = \rho_0\frac{\partial\Psi}{\partial\mathbf{E}^e} = 2f_{dev}(d)G\,\mathbf{E}^e_{dev} + f_{vol}(d)K\mathrm{tr}[\mathbf{E}^e]\,\mathbf{1},\\
&2.\quad {}^pQ_i = \rho_0\frac{\partial\Psi}{\partial{}^pq_i} = H_i\,{}^pq_i, \quad i = 1, 2\\
&3.\quad \hat{a} = \rho_0\frac{\partial\Psi}{\partial\phi} = {}^{\chi}H(\phi-d),\\
&4.\quad \boldsymbol{\zeta} = \rho_0\frac{\partial\Psi}{\partial\boldsymbol{H}} = {}^{\chi}A\,\boldsymbol{H},\\
&5.\quad Y_d = -\rho_0\frac{\partial\Psi}{\partial d} = -(f'_{dev}(d)G\mathbf{E}^e_{dev} : \mathbf{E}^e_{dev} + f'_{vol}(d)\frac{K}{2}\left(\mathrm{tr}\left[\mathbf{E}^e\right]\right)^2) + {}^{\chi}H(\phi-d),\\
&6.\quad {}^dQ_i = \rho_0\frac{\partial\Psi}{\partial{}^dq_i} = H_{di}\,{}^dq_i, \quad i = 1, 2.
\end{aligned}
\tag{16}
$$

Here the first two terms of the Eq. ((16).1) are the deviatoric and volumetric parts of the Hill stress under elastic deformation, and the quantities ${}^pQ_1$ and ${}^pQ_2$ in Eq. ((16).2) refer to stress like internal variables and are responsible for the softening and hardening of the material, respectively. Eqs. ((16).3) and ((16).4) represent the microforce and microstress vector, respectively. Y_d in Eq. ((16).5) is damage driving force and the quantities ${}^dQ_1$ and ${}^dQ_2$ in Eq. ((16).6) are damage hardening, respectively.

Now, the dissipation inequality (11) reads as

$$
\mathcal{D}^{\mathrm{me}} = (\mathbf{S} - \mathbf{T} : \mathbb{P}) : \mathbf{D} + \mathbf{T} : \dot{\mathbf{E}}^p - {}^p\underline{Q}\cdot{}^p\underline{\dot{q}} + Y_d\dot{d} - {}^d\underline{Q}\cdot{}^d\underline{\dot{q}} \geq 0. \tag{17}
$$

Applying the Coleman–Noll procedure, requiring that the dissipation inequality (17) should be valid for all processes, including $\mathbf{D} = \mathbf{0}$ and $\dot{\boldsymbol{H}} = \mathbf{0}$. Therefore, as a necessary condition we conclude

$$
1.\quad (\mathbf{S} - \mathbf{T} : \mathbb{P}) : \mathbf{D} = 0 \quad \Longrightarrow \quad 2.\quad \mathbf{S} = \mathbb{P} : \mathbf{T}, \tag{18}
$$

and the reduced form of the inequality (17) becomes

$$D^{red} = \mathbf{T} : \dot{\mathbf{E}}^p - {}^{p}\underline{Q}\ {}^{p}\dot{\underline{q}} + Y_d\ \dot{d} - {}^{d}\underline{Q}\ {}^{d}\dot{\underline{q}} \geq 0. \tag{19}$$

The thermodynamic consistency is discussed in Appendix A.

The coupled strong form for the initial boundary value problem is obtained from Eq. (8) as

$$\begin{aligned}
&1. && -\operatorname{Div}\mathbf{P}[\mathbf{u},\phi] && = \boldsymbol{b} && \mathbf{X}\in\mathscr{B}\\
&2. && \hat{a}[\mathbf{u},\phi] - \operatorname{Div}\boldsymbol{\zeta}[\phi] && = m[\phi] && \mathbf{X}\in\mathscr{B}\\
&3. && \mathbf{P}\cdot\mathbf{N} && = \bar{\boldsymbol{T}} && \mathbf{X}\in\partial\mathscr{B}_\sigma\\
&4. && \mathbf{u} && = \bar{\mathbf{u}} && \mathbf{X}\in\partial\mathscr{B}_v\\
&5. && \boldsymbol{\zeta}\cdot\mathbf{N} && = \bar{T}_m && \mathbf{X}\in\partial\mathscr{B}_\zeta\\
&6. && \phi && = \bar{\phi} && \mathbf{X}\in\partial\mathscr{B}_\phi.
\end{aligned} \tag{20}$$

Here $\mathbf{P} = \mathbf{F}\cdot\mathbf{S}$ is the first Piola–Kirchhoff stress tensor. The equilibrium conditions Eq. ((20).1–2) constitute a coupled problem due to the dependence on the primary fields $\mathbf{u}$ and ϕ. $\partial\mathscr{B}_\sigma$, $\partial\mathscr{B}_v$, $\partial\mathscr{B}_\zeta$, and $\partial\mathscr{B}_\phi$ are Neumann and Dirichlet boundary conditions for the micro and macro problems, respectively. We assume that the micromorphic tractions satisfy $\bar{T}_m = 0$.

By aid of Eqs. ((1).2) and ((16).4), ((20).2) rewrites as

$$\begin{aligned}
&{}^{\chi}H(\phi - d) - \operatorname{Div}\boldsymbol{\zeta} = {}^{\chi}H(\phi - d) - {}^{\chi}A\operatorname{Div}(\partial_{\mathbf{X}}\phi) = 0\\
&\quad\Longrightarrow \phi - l_c^2\Delta_{\mathbf{X}}\phi = d \quad \in\mathscr{B}, \quad \text{with} \quad l_c^2 = \frac{{}^{\chi}A}{{}^{\chi}H}.
\end{aligned} \tag{21}$$

Here, $\Delta_{\mathbf{X}} = \operatorname{Div}\partial_{\mathbf{X}}$ is the Laplace operator and l_c is an internal characteristic length scale, that governs the gradient effect. This length scale is real positive, given that the parameters ${}^{\chi}A$ and ${}^{\chi}H$ are positive.

2.3. Damage and plasticity evolution

In Lemaitre-type isotropic damage in Lemaitre (1985), the macroscopic stress acting on the damaged configuration is reduced because the load-bearing area decreases as damage grows. A standard way to preserve a physically meaningful driving force for plastic flow is to work with an effective stress that refers to the undamaged configuration. In the present formulation, the effective deviatoric stress tensor $\tilde{\mathbf{T}}_{dev}$, which is related to the undamaged cross-section area, is defined as

$$\tilde{\mathbf{T}}_{dev} = f_{dev}^{-1}(d)\mathbf{T}_{dev} = 2G\ \mathbf{E}^e_{dev} \quad . \tag{22}$$

For numerical stability, we perform a modification for the function f_{dev}, namely

$$f_{dev}(d) = \frac{\exp(-\eta_{dev}d) + \epsilon}{1+\epsilon}, \tag{23}$$

where $\epsilon = 10^{-5}$.

Glassy polymers exhibit shear yielding before rupture, and damage occurs only after a threshold is reached. To reflect this behavior, the model adopts two distinct activation mechanisms: a plastic surface governed by the equivalent stress σ_v and the plastic resistance ${}^{p}Q$, and a damage surface governed by the damage driving force Y_d and the corresponding resistance ${}^{d}Q$. By aid of the Hill stress tensor in Eq. (22) we define the equivalent von Mises stress, the stress-like internal variables, the damage hardening variables, the plastic potential and damage potential

$$\begin{aligned}
&1. && \sigma_v && = \sqrt{\frac{3}{2}}\|\tilde{\mathbf{T}}_{dev}\|,\\
&2. && {}^{p}Q && = \sum_{i=1}^{2} {}^{p}Q_i = {}^{p}Q_1 + {}^{p}Q_2,\\
&3. && {}^{d}Q && = \sum_{i=1}^{2} {}^{d}Q_i = {}^{d}Q_1 + {}^{d}Q_2,\\
&4. && \boldsymbol{\Phi}_p && = \left(\left(\frac{\sigma_v}{{}^{p}Q}\right)^{m_p} - 1\right){}^{p}Q,\\
&5. && \boldsymbol{\Phi}_d && = \left(\left(\frac{Y_d}{{}^{d}Q}\right)^{m_d} - 1\right){}^{d}Q.
\end{aligned} \tag{24}$$

The quantities ${}^{p}Q_1$ and ${}^{p}Q_2$ are the stress-like internal variables in Eq. ((16).2). The quantities ${}^{d}Q_1$ and ${}^{d}Q_2$ are the internal damage hardening variables in Eq. ((16).3). m_p and m_d are material parameters.

The present work also adopts a double-surface framework but goes beyond existing approaches by introducing a thermally activated, rate-dependent damage evolution based on an Arrhenius-type formulation. This extension enables a physically motivated description of time-dependent damage processes, which will be further investigated in future experimental studies. Plasticity evolution and damage in glassy polymers are rate-dependent and thermally activated processes. Therefore, the plastic flow and damage multipliers $\dot{\lambda}_p$ and $\dot{\lambda}_d$ are defined using an Arrhenius-type formulation as

$$\begin{aligned}
&1. && \dot{\lambda}_p && = \dot{\lambda}_{p0}\exp\left(\frac{A_p}{\theta}\boldsymbol{\Phi}_p\right) && = \dot{\lambda}_{p0}\exp\left(\frac{A_p\,{}^{p}Q}{\theta}\left(\left(\frac{\sigma_v}{{}^{p}Q}\right)^{m_p} - 1\right)\right),\\
&2. && \dot{\lambda}_d && = \dot{\lambda}_{d0}\exp\left(\frac{A_d}{\theta}\boldsymbol{\Phi}_d\right) && = \dot{\lambda}_{d0}\exp\left(\frac{A_d\,{}^{d}Q}{\theta}\left(\left(\frac{Y_d}{{}^{d}Q}\right)^{m_d} - 1\right)\right),
\end{aligned} \tag{25}$$

where $\dot{\lambda}_{p0}$, $\dot{\lambda}_{d0}$, A_p, and A_d are material parameters and θ is the absolute temperature. Additionally, we define the evolution equations for the internal variables q_{p_i} and internal damage variables q_{d_i} in Eq. (12) as

$$\begin{aligned} 2.\quad {}^{p}\dot{q}_1 &= \dot{\lambda}_p\left(1-\frac{{}^{p}Q_1}{{}^{p}Q^*{}_1}\right),\\ 3.\quad {}^{p}\dot{q}_2 &= \dot{\lambda}_p,\\ 4.\quad {}^{d}\dot{q}_1 &= \dot{\lambda}_d\left(1-\frac{{}^{d}Q_1}{{}^{d}Q^*{}_1}\right),\\ 5.\quad {}^{d}\dot{q}_2 &= \dot{\lambda}_d. \end{aligned} \tag{26}$$

Here, ${}^{p}Q^*{}_1$, and ${}^{d}Q^*{}_1$ are material parameters.

Furthermore, we define the evolution equations for the plastic part $\mathbf{E}^p$ in Eq. (7) and the damage variable d in Eq. (12) with the help of Φ_p and Φ_d in Eq. (24) as

$$\begin{aligned} 1.\quad \dot{\mathbf{E}}^p &= \dot{\lambda}_p\frac{\partial\Phi_p}{\partial\mathbf{T}} = f_{dev}^{-1}(d)\dot{\lambda}_p m_p\left(\frac{\sigma_v}{{}^{p}Q}\right)^{m_p-1}\sqrt{\frac{3}{2}}\mathbf{N}, \qquad \text{where}\ \ \mathbf{N}=\frac{\tilde{\mathbf{T}}_{dev}}{\|\tilde{\mathbf{T}}_{dev}\|}=\frac{\mathbf{T}_{dev}}{\|\mathbf{T}_{dev}\|},\\ 2.\quad \dot{d} &= \dot{\lambda}_d\frac{\partial\Phi_d}{\partial Y_d} = \dot{\lambda}_d m_d\left(\frac{Y_d}{{}^{d}Q}\right)^{m_d-1}. \end{aligned} \tag{27}$$

The time derivatives of the thermodynamic forces in the equations are calculated by inserting the evolution Eqs. ((26).1), ((26).2), ((26).3) Eq. ((26).4) into Eq. (16), so that

$$\begin{aligned} 1.\quad {}^{p}\dot{Q}_1 &= H_{p1}\dot{\lambda}_p\left(1-\frac{{}^{p}Q_1}{{}^{p}Q^*{}_1}\right), \quad \text{with} \quad {}^{p}Q_1[t=0]=Q_{p0}\\ 2.\quad {}^{p}\dot{Q}_2 &= H_{p2}\dot{\lambda}_p, \quad \text{with} \quad {}^{p}Q_2[t=0]=0,\\ 3.\quad {}^{d}\dot{Q}_1 &= H_{d1}\dot{\lambda}_d\left(1-\frac{{}^{d}Q_1}{{}^{d}Q^*{}_1}\right), \quad \text{with} \quad {}^{d}Q_1[t=0]=Q_{d0}\\ 4.\quad {}^{d}\dot{Q}_2 &= H_{d2}\dot{\lambda}_d, \quad \text{with} \quad {}^{d}Q_2[t=0]=0. \end{aligned} \tag{28}$$

Here, Q_{p0}, and Q_{d0} represent the threshold values for plastic flow and damage initiation, respectively.

By aid of Eq. ((27).1) the rate of equivalent plastic strain $\dot{e}_v$ becomes

$$\dot{e}_v=\sqrt{\frac{2}{3}\dot{\mathbf{E}}^p:\dot{\mathbf{E}}^p}=f_{dev}^{-1}(d)\dot{\lambda}_p m_p\left(\frac{\sigma_v}{{}^{p}Q}\right)^{m_p-1}. \tag{29}$$

Remarks

1. Note, that the flow parameter $\dot{\lambda}_p$ in Eq. (25) is always non-negative, which has some consequences for the proof on thermodynamic consistency presented later.
2. By aid of the Hill stress $\mathbf{T}$ and the inelastic strain rate in the relations ((27).1) we obtain

$$1.\quad \mathbf{T}:\dot{\mathbf{E}}^p=\mathbf{T}:f_{dev}^{-1}(d)\dot{\lambda}_p m_p\left(\frac{\sigma_v}{{}^{p}Q}\right)^{m_p-1}\sqrt{\frac{3}{2}}\frac{\mathbf{T}_{dev}}{\|\mathbf{T}_{dev}\|}=\dot{\lambda}_p m_p\left(\frac{\sigma_v}{{}^{p}Q}\right)^{m_p-1}\sigma_v. \tag{30}$$

3. In Eq. (28), ${}^{p}Q_1$ and ${}^{p}Q_2$ define softening and hardening, respectively. For ${}^{p}Q^*{}_1 > Q_0$, ${}^{p}Q_1$ is negative and consequently softening takes place. The quantity ${}^{p}Q_2$ is a monotonically increasing function and represents hardening.
4. Following Mahnken and Dammann (2014) and Mahnken and Shaban (2013), we set $m_p=\frac{5}{6}$. Therefore, under our consistent double-surface damage–plasticity formulation, we also take $m_d=\frac{5}{6}$.

2.4. Damage asymmetric effect

Glassy polymers show pronounced asymmetry in the mechanical behavior between tension and compression, where damage initiates and progresses under tensile loading. However the material exhibits higher resistance to degradation under compression. Following Mahnken (2003), Each stress mode is associated with a distinct weighting function, enabling the model to apply varying activation levels based on whether the stress state is tensile or compressive.

In this work, those weighting functions depend on the stress mode factor ξ, where

$$1.\quad \xi=\frac{\sqrt{27}}{3}\frac{J_3}{{J_2}^{3/2}}, \quad 2.\quad J_i=\frac{1}{i}\mathbf{1}:(\mathbf{T}_{dev})^i. \tag{31}$$

Here, the stress mode $j=1,2,\ldots,S$ can be investigated, for example, in tension, compression, and shear, respectively. The specific mathematical structures for weighting functions have been in Mahnken (2003) formulated on the basis of the quantities

$$1.\quad \sum_{i=1}^{S} w_i[\xi]=1. \tag{32}$$

For the stress modes related to loading scenarios of tension and compression, we set $S=2$. Then, the requirements (32) are satisfied by the following weighting functions in terms of the stress mode factor ξ

$$\begin{aligned} 1.\quad &\text{tension}: & w_1[\xi] &= \frac{1}{2}(1+\xi),\\ 2.\quad &\text{compression}: & w_2[\xi] &= \frac{1}{2}(1-\xi). \end{aligned} \tag{33}$$

Table 1
Constitutive relations for finite elasto-plasticity with gradient term.

I. Kinematics

$$\begin{aligned}
&1.\quad \boldsymbol{H} = \partial_{\mathbf{X}}\phi,\\
&2.\quad \mathbf{F} = \partial_{\mathbf{X}}\boldsymbol{\varphi},\\
&3.\quad \mathbf{C} = \mathbf{F}^t \cdot \mathbf{F},\\
&4.\quad \mathbf{E} = \mathbf{E}^e + \mathbf{E}^p, \quad \text{where} \quad \mathbf{E} = \frac{1}{2}\ln[\mathbf{C}], \quad \mathrm{tr}\mathbf{E}^e = \mathbf{E}^e : \mathbf{1}, \quad \mathbf{E}^e_{dev} = \mathbf{E}^e - \frac{1}{3}\mathrm{tr}[\mathbf{E}^e]\mathbf{1}
\end{aligned} \tag{35}$$

II. Energy function

$$\begin{aligned}
&\rho_0\Psi = \rho_0\Psi^{vol} + \rho_0\Psi^{iso} + \rho_0\Psi^{p} + \rho_0\Psi^{nloc}\\
&= f_{dev}(d)G\mathbf{E}^e_{dev} : \mathbf{E}^e_{dev} + f_{vol}(d)K\,(\mathrm{tr}\,[\mathbf{E}^e])^2 + \sum_{i=1}^{n=2}\frac{1}{2}\,H_i\,{}^{p}q_i^2 + \frac{1}{2}\,{}^{\chi}H\,(\phi - d)^2 + \frac{{}^{\chi}A}{2}\boldsymbol{H}\cdot\boldsymbol{H} + \sum_{i=1}^{n=2}\frac{1}{2}\,H_{d\,i}\,{}^{d}q_i^2
\end{aligned} \tag{36}$$

III. Evolution of the stress like internal variables and internal damage hardening variables

$$\begin{aligned}
&1.\quad {}^{p}\dot{Q}_1 = H_{p1}\dot{\lambda}_p\left(1 - \frac{{}^{p}Q_1}{{}^{p}Q^*_1}\right)\\
&2.\quad {}^{p}\dot{Q}_2 = H_{p2}\dot{\lambda}_p\\
&3.\quad {}^{p}Q = {}^{p}Q_1 + {}^{p}Q_2\\
&4.\quad {}^{d}\dot{Q}_1 = H_{d1}\dot{\lambda}_d\left(1 - \frac{{}^{d}Q_1}{{}^{d}Q^*_1}\right)\\
&5.\quad {}^{d}\dot{Q}_2 = H_{d2}\dot{\lambda}_d,\\
&6.\quad {}^{d}Q = {}^{d}Q_1 + {}^{d}Q_2
\end{aligned} \tag{37}$$

IV. Forces and stresses

$$\begin{aligned}
&1.\ \mathbf{T} = \mathbf{T}_{vol} + \mathbf{T}_{dev}, \quad \text{where} \quad \mathbf{T}_{vol} = f_{vol}(d)K\,\mathrm{tr}\,[\mathbf{E}^e]\,\mathbf{1}, \quad \mathbf{T}_{dev} = 2f_{dev}(d)G\mathbf{E}^e_{dev},\\
&2.\ \tilde{\mathbf{T}}_{dev} = f^{-1}_{dev}(d)\mathbf{T}_{dev} = 2G\mathbf{E}^e_{dev},\\
&3.\ \hat{a} = {}^{\chi}H(\phi - d)\\
&4.\ \boldsymbol{\zeta} = {}^{\chi}A\ \boldsymbol{H}\\
&5.\ Y_d = -(f'_{dev}(d)G\mathbf{E}^e_{dev} : \mathbf{E}^e_{dev} + f'_{vol}(d)\frac{K}{2}\left(\mathrm{tr}\left[\mathbf{E}^e\right]\right)^2) + {}^{\chi}H\,(\phi - d)
\end{aligned} \tag{38}$$

V. Flow direction and flow factor

$$\begin{aligned}
&1.\ \mathbf{N} = \frac{\tilde{\mathbf{T}}_{dev}}{||\tilde{\mathbf{T}}_{dev}||}\\
&2.\ \dot{\lambda}_p = \dot{\lambda}_{p0}\exp\left(\frac{A_p\,{}^{p}Q}{\theta}\left(\left(\frac{\sigma_v}{{}^{p}Q}\right)^{m_p} - 1\right)\right), \quad \text{where} \quad \sigma_v = \sqrt{\frac{3}{2}}||\tilde{\mathbf{T}}_{dev}||
\end{aligned} \tag{39}$$

VI. Inelastic strain evolution

$$\dot{\mathbf{E}}^p = \dot{\lambda}_p\frac{\partial\boldsymbol{\Phi}_p}{\partial\mathbf{T}} = f^{-1}_{dev}(d)\dot{\lambda}_p m_p\left(\frac{\sigma_v}{{}^{p}Q}\right)^{m_p-1}\sqrt{\frac{3}{2}}\mathbf{N}, \qquad \dot{e}_v = \sqrt{\frac{2}{3}\dot{\mathbf{E}}^p : \dot{\mathbf{E}}^p} = f^{-1}_{dev}(d)\dot{\lambda}_p m_p\left(\frac{\sigma_v}{{}^{p}Q}\right)^{m_p-1} \tag{40}$$

VII. Damage evolution

$$\begin{aligned}
&1.\quad \dot{\lambda}_d = \dot{\lambda}_{d0}\exp\left(\frac{A_d\,{}^{d}Q}{\theta}\left(\left(\frac{Y_d}{{}^{d}Q}\right)^{m_d} - 1\right)\right)\\
&2.\quad \dot{d} = \dot{d} = \dot{\lambda}_d\frac{\partial\boldsymbol{\Phi}_d}{\partial Y_d} = \dot{\lambda}_d m_d\left(\frac{Y_d}{{}^{d}Q}\right)^{m_d-1},
\end{aligned} \tag{41}$$

VIII. Material parameters

$$\underline{\kappa}_j = \left[K, G, \dot{\lambda}_{p0}, A_p, Q_0, {}^{p}Q^*_1, H_{p1}, H_{p2}, {}^{d}Q^*_1, H_{d1}, H_{d2}, \dot{\lambda}_{d0i}, A_{di}, Q_{d0i}, \eta_{vol_i}, \eta_{dev_i}, \{i = 1,2\}, {}^{\chi}A, {}^{\chi}H, m_p, m_d\right]^T \tag{42}$$

The set of weighted material parameters used in this study to capture the asymmetric effect is

$$\begin{aligned}
&1.\quad \eta_{vol} = \sum_{i=1}^{S} w_i[\xi]\eta_{vol_i},\\
&2.\quad \eta_{dev} = \sum_{i=1}^{S} w_i[\xi]\eta_{dev_i},\\
&3.\quad Q_{d0} = \sum_{i=1}^{S} w_i[\xi]Q_{d0i},\\
&4.\quad A_d = \sum_{i=1}^{S} w_i[\xi]A_{di},\\
&5.\quad \dot{\lambda}_{d0} = \sum_{i=1}^{S} w_i[\xi]\dot{\lambda}_{d0i}.
\end{aligned} \tag{34}$$

2.5. Summary of constitutive equations

The complete set of equations is summarized in Table 1: The standard additive decomposition of the total strain tensor $\mathbf{E}$ is introduced in Eq. I. Eq. II specifies the energy function Ψ, which is split into an elastic volumetric part Ψ^{vol}, an elastic isochoric part Ψ^{iso}, a plastic part Ψ^{p} and a nonlocal part Ψ^{nloc} related to damage evolution and regularization. The parameters K and G denote the bulk and shear modulus, respectively taking into account that $G = G[E, \nu]$, where E is Young's modulus and ν is Poisson's ratio. In the nonlocal part ${}^{\chi}A$ is a micromorphic stiffness and ${}^{\chi}H$ is a penalty term forcing proximity between d and ϕ. The thermodynamic forces Q_{p_1}, Q_{p_2}, Q_{d1}, and Q_{d2} are given in Eq. III, and Eq. IV summarizes the different stress tensors. The flow direction $\mathbf{N}$, the flow multiplier and the von Mises stress are presented in Eq. V, where the evolution of the inelastic strain tensor $\dot{\mathbf{E}}^p$ is given in Eq. VI. In Eq. VII damage evolution is presented. Finally, Eq. VIII in Table 1 summarizes all material parameters.

3. Algorithmic implementation

3.1. Weak formulation and linearization

To construct the weak form of the problem in Eq. ((20).1) we multiply the linear momentum and micromorphic balance equations by the corresponding vectorial and scalar test functions $\delta\mathbf{u}$ and $\delta\phi$, respectively. By considering the boundary condition Eqs. ((20).3) and ((20).5), integrating over domain $\mathscr{B}$ and applying divergence theorem, the weak formulation is obtained as:

$$\begin{aligned} &1.\quad \mathcal{R}_{\mathbf{u}}[\mathbf{u},\phi;\delta\mathbf{u}] = f_u^{\text{int}}[\mathbf{u},\phi;\delta\mathbf{u}] - f_u^{\text{ext}}[\delta\mathbf{u}] = \langle \mathbf{S} : \mathbf{F}^T\partial_{\mathbf{X}}\delta\mathbf{u}\rangle_{\mathscr{B}} - \langle \delta\mathbf{u}\cdot\boldsymbol{b}\rangle_{\mathscr{B}} - \langle \delta\mathbf{u}\cdot\bar{\boldsymbol{T}}\rangle_{\partial\mathscr{B}} = \mathbf{0} \\ &2.\quad \mathcal{R}_{\phi}[\mathbf{u},\phi;\delta\phi] = f_\phi^{\text{int}}[\mathbf{u},\phi;\delta\phi] - f_\phi^{\text{ext}}[\delta\mathbf{u}] = \langle \boldsymbol{\zeta}\cdot\partial_{\mathbf{X}}\delta\phi + \hat{a}\delta\phi\rangle_{\mathscr{B}} - \langle \delta\phi m\rangle_{\mathscr{B}} - \langle \delta\phi\bar{T}_m\rangle_{\partial\mathscr{B}} = 0 \end{aligned} \tag{43}$$

where $f_\bullet^{\text{int}}$ and $f_\bullet^{\text{ext}}$ are the internal and external works, respectively.

The highly non-linear system of Eqs. (43) is linearized with respect to the global unknowns $\mathbf{u}$ and ϕ using Gâteaux derivative, see e.g. Marsden and Hughes (1994), and solved iteratively using Newton method for the increments $\Delta\mathbf{u}$ and $\Delta\phi$

$$\begin{aligned} &1.\quad \mathcal{R}_{\mathbf{u}}[\mathbf{u},\phi;\delta\mathbf{u}] = \mathcal{R}_{\mathbf{u}}[\mathbf{u},\phi;\delta\mathbf{u}] + D_{\mathbf{u}}\mathcal{R}_{\mathbf{u}}[\mathbf{u},\phi;\delta\mathbf{u}]\Delta\mathbf{u} + D_\phi\mathcal{R}_{\mathbf{u}}[\mathbf{u},\phi;\delta\mathbf{u}]\Delta\phi = \mathbf{0}, \\ &2.\quad \mathcal{R}_{\phi}[\mathbf{u},\phi;\delta\mathbf{u}] = \mathcal{R}_{\phi}[\mathbf{u},\phi;\delta\mathbf{u}] + D_{\mathbf{u}}\mathcal{R}_{\phi}[\mathbf{u},\phi;\delta\mathbf{u}]\Delta\mathbf{u} + D_\phi\mathcal{R}_{\phi}[\mathbf{u},\phi;\delta\mathbf{u}]\Delta\phi = 0. \end{aligned} \tag{44}$$

In the reference configuration, the tangent forms appearing in Eq. (44) take the following closed form:

$$\begin{aligned} &1.\quad D_{\mathbf{u}}\mathcal{R}_{\mathbf{u}}[\mathbf{u},\phi;\delta\mathbf{u}]\cdot\Delta\mathbf{u} = \langle(\mathbb{C}^1 : \mathbf{F}^T\cdot\partial_{\mathbf{X}}\Delta\mathbf{u}) : \mathbf{F}^T\cdot\partial_{\mathbf{X}}\delta\mathbf{u} + (\partial_{\mathbf{X}}\Delta\mathbf{u}\cdot\mathbf{S} : \partial_{\mathbf{X}}\delta\mathbf{u})\rangle_{\mathscr{B}} \\ &2.\quad D_\phi\mathcal{R}_{\mathbf{u}}[\mathbf{u},\phi;\delta\mathbf{u}]\cdot\Delta\phi = \langle(\mathbb{C}^2\Delta\phi : \partial_{\mathbf{X}}\delta\mathbf{u})\rangle_{\mathscr{B}} \\ &3.\quad D_{\mathbf{u}}\mathcal{R}_{\phi}[\mathbf{u},\phi;\delta\phi]\cdot\Delta\mathbf{u} = \langle(\mathbb{C}^{31} : \mathbf{F}^T\cdot\partial_{\mathbf{X}}\Delta\mathbf{u})\cdot\partial_{\mathbf{X}}\delta\phi + (\mathbb{C}^{32} : \mathbf{F}^T\cdot\partial_{\mathbf{X}}\Delta\mathbf{u})\delta\phi\rangle_{\mathscr{B}} \\ &4.\quad D_\phi\mathcal{R}_{\phi}[\mathbf{u},\phi;\delta\phi]\cdot\Delta\phi = \langle(\mathbb{C}^{41}\cdot\partial_{\mathbf{X}}\Delta\phi)\cdot\partial_{\mathbf{X}}\delta\phi + (\mathbb{C}^{42}\Delta\phi)\delta\phi\rangle_{\mathscr{B}} \end{aligned} \tag{45}$$

in which the algorithmic tangent moduli are defined

$$1.\quad \mathbb{C}^1 = 2\frac{\partial\mathbf{S}}{\partial\mathbf{C}} \quad 2.\quad \mathbb{C}^2 = \frac{\partial\mathbf{S}}{\partial\phi} \quad 3.\quad \mathbb{C}^{31} = 2\frac{\partial\boldsymbol{\zeta}}{\partial\mathbf{C}},\quad \mathbb{C}^{32} = 2\frac{\partial\hat{a}}{\partial\mathbf{C}} \quad 4.\quad \mathbb{C}^{41} = \frac{\partial\boldsymbol{\zeta}}{\partial\boldsymbol{H}},\quad \mathbb{C}^{42} = \frac{\partial\hat{a}}{\partial\phi}. \tag{46}$$

A detailed derivation of the tangent moduli is provided in the Appendices.

3.2. Spatial discretization

In line with the standard approximations of the finite element method, the geometry of each spatial element $\mathscr{B}^e$, with respect to the reference and the current configurations, is approximated as

$$\begin{aligned} &1.\ \mathbf{X} = \sum_{a=1}^{n_{\text{node}}} \mathbf{X}^e{}_a\, N_a(\underline{\xi}), \\ &2.\ \mathbf{x} = \sum_{a=1}^{n_{\text{node}}} \mathbf{x}^e{}_a\, N_a(\underline{\xi}), \\ &3.\ \phi = \sum_{a=1}^{n_{\text{node}}} \phi^e{}_a\, N_a(\underline{\xi}). \end{aligned} \tag{47}$$

Here n_{node} is the number of nodes per element, N_a are the shape functions, and $\mathbf{X}^e{}_a$, $\mathbf{x}^e{}_a$, $\phi^e{}_a$ are the corresponding nodal values. The gradients in Eqs. (1) and (2) become

$$\begin{aligned} &1.\ \mathbf{F} = \sum_{a=1}^{n_{\text{node}}} \mathbf{x}^e{}_a \otimes \partial_{\mathbf{X}} N_a(\underline{\xi}) = [\mathbf{F}]_{iI}\,\mathbf{e}_i\otimes\mathbf{e}_I, \\ &2.\ \boldsymbol{H} = \sum_{a=1}^{n_{\text{node}}} \phi^e{}_a \otimes \partial_{\mathbf{X}} N_a(\underline{\xi}) = [\boldsymbol{H}]_{iI}\,\mathbf{e}_i\otimes\mathbf{e}_I. \end{aligned} \tag{48}$$

Then, the residuals Eq. (44) as well as the tangent forms in Eq. (45) are given for each finite element $\mathscr{B}_e$ in Appendix B.

3.3. Time integration of evolution equations

This section is concerned with numerical integration of the rate-equation for $\mathbf{E}^p, \dot{e}_v$ and $\dot{d}$ and in Table 1. Following standard integration procedures in finite element techniques a *strain-driven* algorithm is considered, where the total gradient ${}^{n+1}\mathbf{F}$ at each time step ${}^{n+1}t$ and initial values $({}^n\mathbf{E}^p, {}^ne_v, {}^nd)$ are given. Then it is the object to find the corresponding quantities $({}^{n+1}\mathbf{E}^p, {}^{n+1}e_v, {}^{n+1}d)$ at time ${}^{n+1}t$ consistent with the constitutive equations in Table 1. To alleviate the notation, from now on the index $n+1$, referring to the actual time step, will be omitted.

For numerical integration of the rate-equations for $\mathbf{E}^p$, $\dot{e}_v$, and $\dot{d}$ summarized in Table 1 an Euler backward rule, which is unconditionally stable, renders the following update scheme

$$\begin{aligned} &1.\ \mathbf{E}^p = {}^n\mathbf{E}^p + \Delta\mathbf{E}^p, \quad \text{where} \quad 2.\ \Delta\mathbf{E}^p = f_{dev}^{-1}(d)\Delta\lambda_p m_p\left(\frac{\sigma_v}{{}^pQ}\right)^{m_p-1}\sqrt{\frac{3}{2}}\mathbf{N}, \quad 3.\ \mathbf{N} = \frac{\tilde{\mathbf{T}}_{dev}}{\|\tilde{\mathbf{T}}_{dev}\|}, \\ &4.\ d = {}^nd + \Delta\lambda_d m_d\left(\frac{Y_d}{{}^dQ}\right)^{m_d-1}, \quad \text{where} \quad 5.\ \Delta d = \Delta\lambda_d m_d\left(\frac{Y_d}{{}^dQ}\right)^{m_d-1} \\ &6.\ e_v = {}^ne_v + \Delta e_v, \quad \text{where} \quad 7.\ \Delta e_v = f_{dev}^{-1}(d)\Delta\lambda_p m_p\left(\frac{\sigma_v}{{}^pQ}\right)^{m_p-1}. \end{aligned} \tag{49}$$

Since $\mathbf{T}_{dev}$ and $\mathbf{T}^{tr}_{dev}$ are coaxial, flow direction in Eq. ((49).-3) renders

$$\frac{\tilde{\mathbf{T}}_{dev}}{\|\tilde{\mathbf{T}}_{dev}\|} = \frac{\mathbf{T}^{tr}_{dev}}{\|\mathbf{T}^{tr}_{dev}\|}. \tag{50}$$

The Hill stress tensor is obtained from the relations

$$\begin{aligned} &1.\quad \mathbf{T} &&= \mathbf{T}_{vol} + \mathbf{T}_{dev}, \quad \text{where} \\ &2.\quad \mathbf{T}_{vol} &&= f_{vol}(d) K \operatorname{tr}(\mathbf{E}^e)\mathbf{1} \\ &3.\quad \mathbf{T}_{dev} &&= f_{dev}(d)\mathbf{T}^{tr}_{dev} - 2G\Delta\lambda_p m_p \left(\frac{\sigma_v}{{}^pQ}\right)^{m_p-1}\sqrt{\frac{3}{2}}\mathbf{N} \\ &4.\quad \mathbf{T}^{tr}_{dev} &&= 2G\left(\mathbf{E}_{dev} - {}^n\mathbf{E}^p\right) \end{aligned} \tag{51}$$

and where $\mathbf{T}^{tr}_{dev}$ is typically referred to as the *trial stress tensor*, see e.g. Simo and Hughes (2006) and references therein. Thus it remains to determine $\Delta\lambda_p$ iteratively as described in the following subsection.

With the help of Eqs. ((51).3) and ((51).4), the effective deviatoric stress tensor $\tilde{\mathbf{T}}_{dev}$ obtain in Eq. (22) renders

$$\tilde{\mathbf{T}}_{dev} = \mathbf{T}^{tr}_{dev} - f^{-1}_{dev}(d) 2G\Delta\lambda_p m_p \left(\frac{\sigma_v}{{}^pQ}\right)^{m_p-1}\sqrt{\frac{3}{2}}\mathbf{N}. \tag{52}$$

3.4. Algorithmic treatment in local iteration

The internal variables $\tilde{\mathbf{T}}_{dev}$ and d appearing in Eqs. (49)–(52) are determined from a coupled nonlinear equation system. Taking the norm of Eq. (52) and invoking the discretized damage update rule from Eq. ((49).4) leads to the unknown vector $\underline{x} = [\,\|\tilde{\mathbf{T}}_{dev}\|,\ d\,]^T$ and the residual system

$$\begin{aligned} &1.\quad \boldsymbol{r} = [r_p, r_d]^T = \mathbf{0}, \\ &2.\quad r_p(\|\tilde{\mathbf{T}}_{dev}\|) = -2G\,\Delta\lambda_p\, f^{-1}_{dev}(d)\, m_p\sqrt{\frac{3}{2}}\left(\frac{\sigma_v}{{}^pQ}\right)^{m_p-1} - \|\tilde{\mathbf{T}}_{dev}\| + \|\mathbf{T}^{tr}_{dev}\|, \\ &3.\quad r_d(d) = d - d_n - \Delta\lambda_d\, m_d\left(\frac{Y_d}{{}^dQ}\right)^{m_d-1}, \end{aligned} \tag{53}$$

where the viscous multipliers read

$$\begin{aligned} &1.\quad \Delta\lambda_p = \Delta t\,\dot{\lambda}_0 \exp\left(\frac{A_p\,{}^pQ}{\theta}\left[\left(\frac{\sigma_v}{{}^pQ}\right)^{m_p} - 1\right]\right), \\ &2.\quad \Delta\lambda_d = \Delta t\,\dot{\lambda}^d_0 \exp\left(\frac{A_d\,{}^dQ}{\theta}\left[\left(\frac{Y_d}{{}^dQ}\right)^{m_d} - 1\right]\right), \end{aligned} \tag{54}$$

and the damage-driving force (from Eqs. (16).5) and (22) is

$$Y_d = -f'_{dev}(d)\, G\left(\frac{\|\tilde{\mathbf{T}}_{dev}\|}{2G}\right)^2 - f'_{vol}(d)\,\frac{K}{2}\left(\operatorname{tr}\left[\mathbf{E}^e\right]\right)^2 + \gamma H(\phi - d). \tag{55}$$

We employ Newton's method

$$\underline{x}^{k+1} = \underline{x}^k - \left(\boldsymbol{J}^k\right)^{-1}\boldsymbol{r}^k, \qquad \boldsymbol{J}^k = \left.\frac{\partial \boldsymbol{r}}{\partial \underline{x}}\right|_{\underline{x}^k}, \qquad k = 0, 1, 2, \ldots \tag{56}$$

with Jacobian

$$\boldsymbol{J} = \begin{bmatrix} J_{11} & J_{12} \\ J_{21} & J_{22} \end{bmatrix} = \begin{bmatrix} \dfrac{\partial r_p}{\partial\|\tilde{T}_{dev}\|} & \dfrac{\partial r_p}{\partial d} \\ \dfrac{\partial r_d}{\partial\|\tilde{T}_{dev}\|} & \dfrac{\partial r_d}{\partial d} \end{bmatrix}. \tag{57}$$

Closed-form expressions for the Jacobian entries are deferred to Appendix C.

4. Numerical examples

4.1. Homogeneous material response

To gain insight into the local behavior of the model, we begin with numerical tests involving homogeneous uniaxial loading. The material response is examined through single-element simulations under tension and compression. Fig. 1.a and b illustrate the geometry and boundary conditions in the front view for tension and compression, respectively. The loading is applied by prescribing a uniform displacement $\bar{u}_x$ at the upper boundary. In addition, symmetry constraints are enforced on the planes $x = 0$, $y = 0$, and $z = 0$. All element edge lengths are 0.5 mm. All numerical examples using single-element rely on the material parameters summarized in Table 2.

The diagrams in Fig. 2 illustrate the homogeneous response of the model under uniaxial loading for different values of the damage threshold parameter Q_{d0}, which governs the initiation and progression of damage. For a given loading history $\bar{u}_x$, lower values of Q_{d0} lead to earlier damage initiation and more pronounced stress softening, as evidenced by the rapid drop in stress after the onset of yielding. In contrast, higher values of Q_{d0} significantly delay damage initiation and maintain higher stress levels for the same strain or displacement conditions, indicating a more

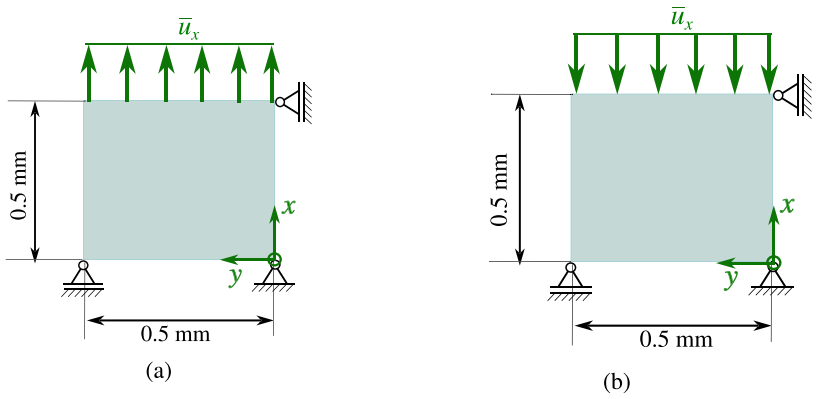

Fig. 1. Dimensions and boundary conditions for a single-element test using an 8-node hexahedral element: (a) Tension test, (b) Compression test.

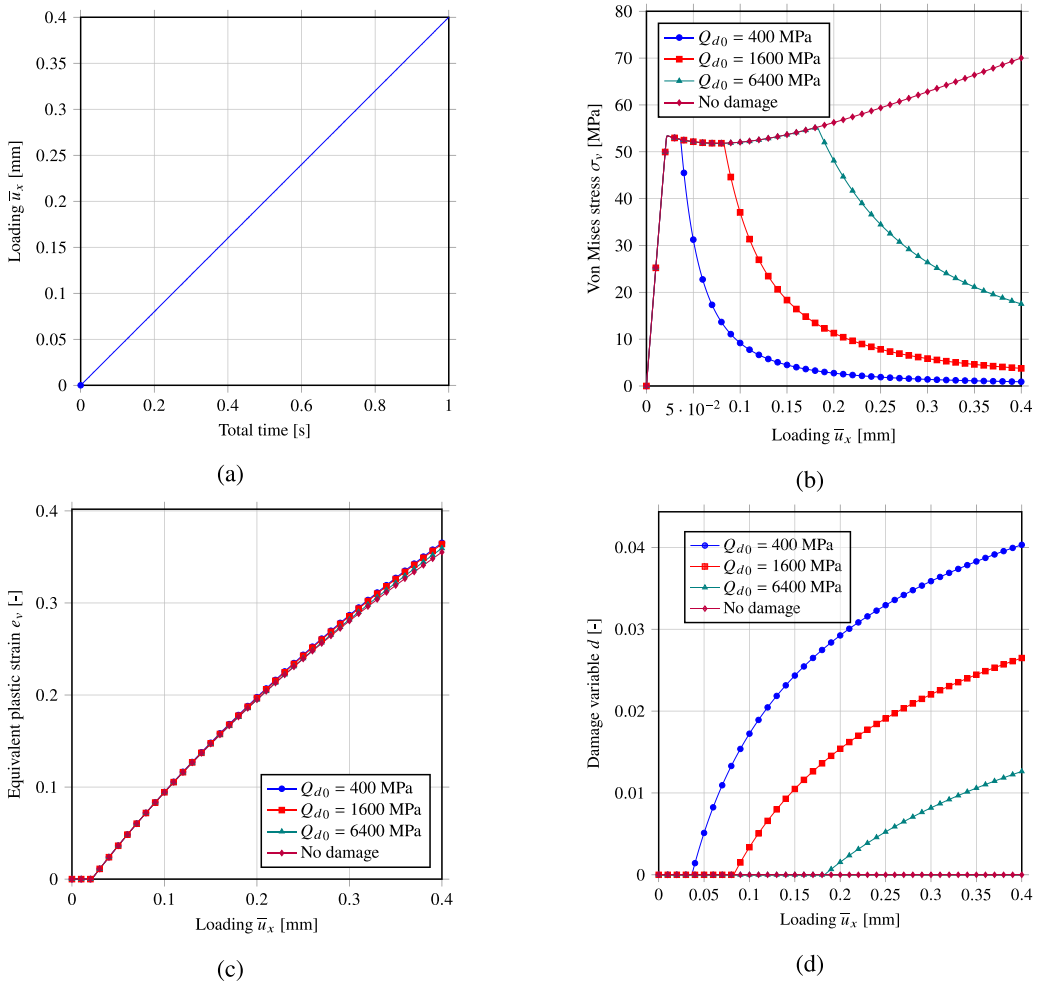

Fig. 2. Homogeneous material response under tensile displacement for varying damage threshold values Q_{d0}: (a) Applied loading $\overline{u}_x$ versus time, (b) Softening behavior due to damage, illustrated by Von Mises Stress σ_v versus the applied loading $\overline{u}_x$; (c) and (d) Evolution of the equivalent plastic strain ϵ_v and damage variable d.

damage-resistant material response. For sufficiently high values of Q_{d0}, stress softening due to damage does not occur within the considered loading range.

Fig. 2.c presents the evolution of plastic strain ϵ_v versus the loading displacement u_x, which shows only slight sensitivity to variations in Q_{d0}, particularly at lower values. This suggests that plasticity is primarily governed by the loading conditions rather than by the evolution of damage. Meanwhile, Fig. 2.d illustrates the accumulation of the damage variable d, where a sharp increase is observed for lower Q_{d0} values, followed by saturation. For higher threshold values, damage accumulates more gradually.

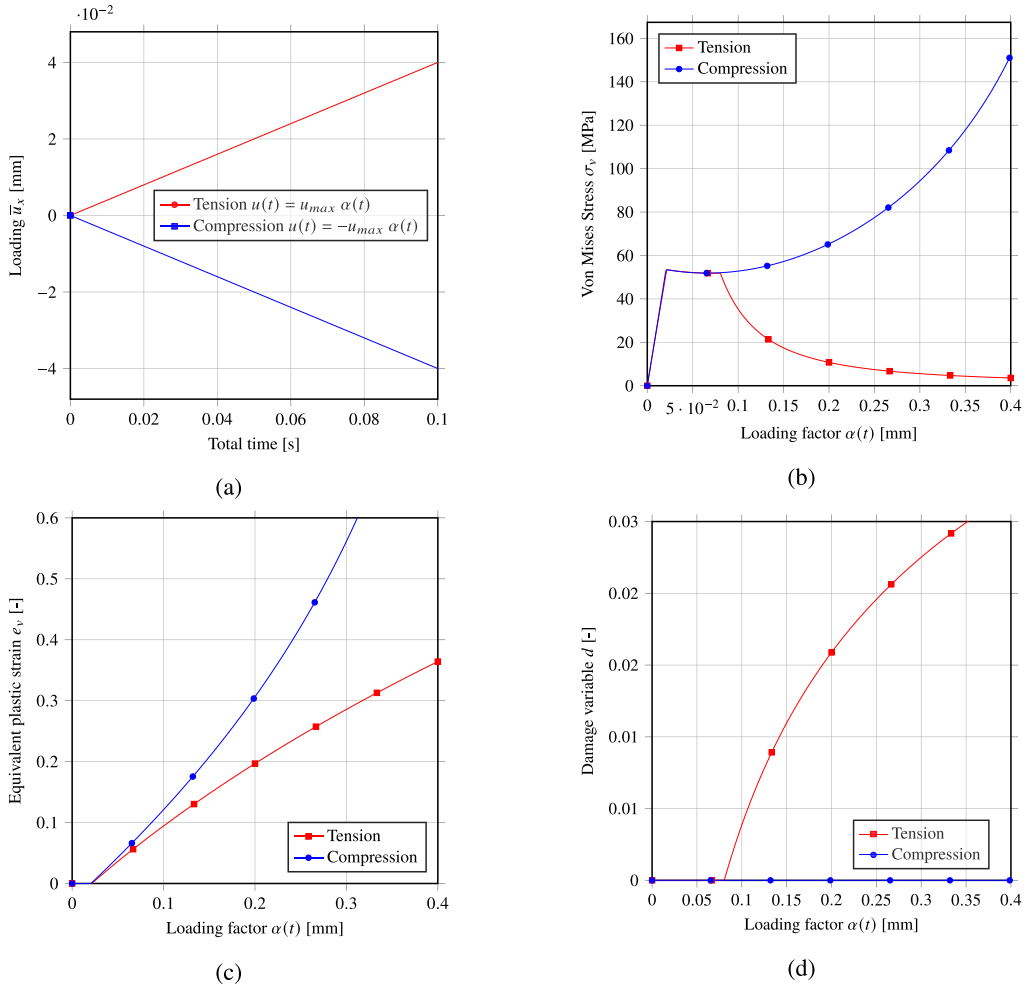

Fig. 3. Homogeneous material response under tension and compression with weighted material parameters from Table 2: (a) Loading history over time, with positive trajectories for tension and negative for compression. (b) Stress response versus the loading factor $\alpha(t)$, noting that stress decreases post-damage in tension and increases continuously under compression. (c) Evolution of plastic strain, highlighting greater deformation under compression compared to tension. (d) Damage variable versus loading factor, showing damage evolving solely under tensile loading.

Table 2
Weighted material parameters used in single-element test.

E [MPa]	θ [K]	ν [−]	$\dot{\lambda}_0$ [s^{-1}]	A_p [K/MPa]	H_1 [MPa]
1643	293.15	0.29	0.1287	140.0	45.797
H_2 [MPa]	Q_0 [MPa]	Q_1^* [MPa]	H_{d1} [MPa]	H_{d2} [MPa]	Q_{d1}^* [MPa]
116.550	53.031	12.3	0.0	100.	12.
Q_{d01} [MPa]	Q_{d02} [MPa]	η_{dev1} [−]	η_{dev2} [−]	η_{vol1} [−]	η_{vol2} [−]
50	3000	100.	0.5	100.	0.5
A_{d1} [K/MPa]	A_{d2} [K/MPa]	$\dot{\lambda}_{d01}$ [s^{-1}]	$\dot{\lambda}_{d02}$ [s^{-1}]	^{4}H	^{4}A
80	8	90.3	0.3	0	0

Fig. 3 illustrates the homogeneous material response under tension and compression, modeled using weighted material parameters from Table 2 to distinguish between the two loading modes. In Fig. 3.a, the loading history over time is depicted, where the loading trajectory is positive in tension and negative in compression.

Fig. 3.b presents the stress response as a of the loading factor $\alpha(t)$, which represents the absolute value of the applied loading $\overline{u}_x$, revealing distinct differences between the two loading modes. Under tensile loading, the stress decreases after damage occurs, as depicted in Fig. 3.d, whereas under compressive loading, the stress rises continuously. Fig. 3.c shows the evolution of plastic strain with respect to the loading factor. The results indicate higher plastic deformation under compression than tension, suggesting that the material undergoes more inelastic deformation when compressed. Finally, Fig. 3.d displays the damage variable as a function of the loading factor. The increase in damage is only pronounced under tensile loading, which is consistent with the results shown in (Fig. 3.b).

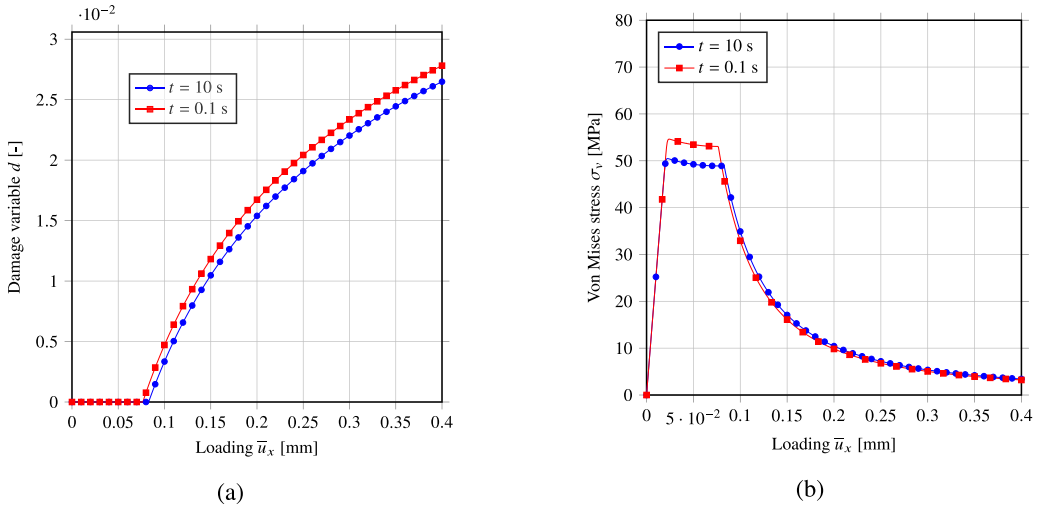

Fig. 4. Homogeneous material response under tensile displacement $\overline{u}_x = 0.4\,\text{mm}$ with varying strain rates $\dot{E}x$ and a constant damage threshold value $Qd0$: (a) Damage evolution over time, showing how the damage variable d changes for two total time of simulation, $t = 10\,\text{s}$ (blue) and $t = 0.1\,\text{s}$ (red). (b) Stress–strain response illustrating the relationship between equivalent von Mises stress σ_v and applied loading u_x, where damage initiation and strain softening due to damage occur earlier at higher strain rates. (For interpretation of the references to color in this figure legend, the reader is referred to the web version of this article.)

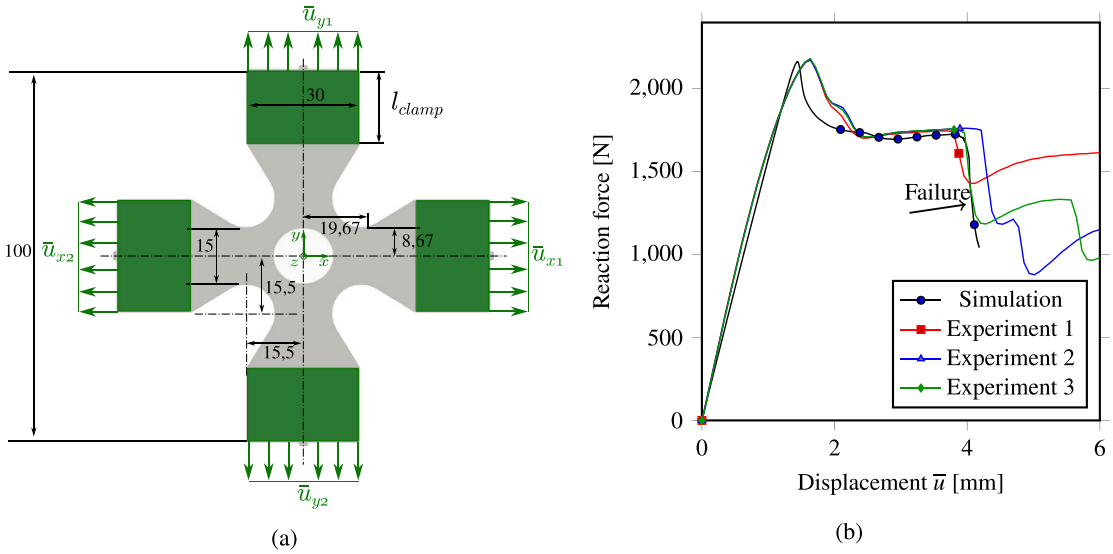

Fig. 5. Model validation against experimental data in Hamdoun and Mahnken (2024b): (a) Geometry and boundary conditions of the cross-shaped specimen; (b) reaction force versus displacement, demonstrating agreement between simulation and experiment.

Fig. 4 illustrates the impact of strain rate on both damage and plasticity evolution. By comparing fast strain rates ($t = 0.1\,\text{s}$), with slow strain rates ($t = 10\,\text{s}$), a clear dependency of damage evolution on strain rate becomes evident. In these simulations, the damage threshold parameter Q_{d0} is held constant.

As shown in Fig. 4.a, at high strain rates, damage progresses significantly more quickly. In contrast, at lower strain rates, the damage variable d accumulates more gradually. Fig. 4.b reveals that the stress–strain response exhibits a slightly higher peak stress at the faster strain rate, reflecting the rate-hardening behavior typical of glassy polymers. Stress softening due to damage also occurs earlier at higher strain rates, consistent with the damage evolution shown in Fig. 4.a. This behavior highlights the coupled nature of viscoplasticity and damage in the model, where the strain rate influences both the stress level in the plastic domain and damage activation.

4.2. Structural finite element examples

We begin by comparing the prototype model introduced in Section 2 against experimental results of the biaxial testing in Hamdoun and Mahnken (2024b) using the specimen in Fig. 5.a. The specimen is made from polycarbonate (Makrolon 3108) with initial dimensions and clamping areas depicted in Fig. 5.a. The tests are conducted on an MTS biaxial machine where the clamping areas are fully constrained while a prescribed, monotonically equibiaxial loading $u(t)$ is applied at each arm of the cross-shaped specimen at a strain rate of $0.1\,\text{s}^{-1}$. The resulting force–displacement data are transferred to a GOM GmbH digital image correlation (DIC) system with two cameras for 3D deformation measurements, along with testing controllers, lighting, and high-performance computers (GOM and Manual, 2011).

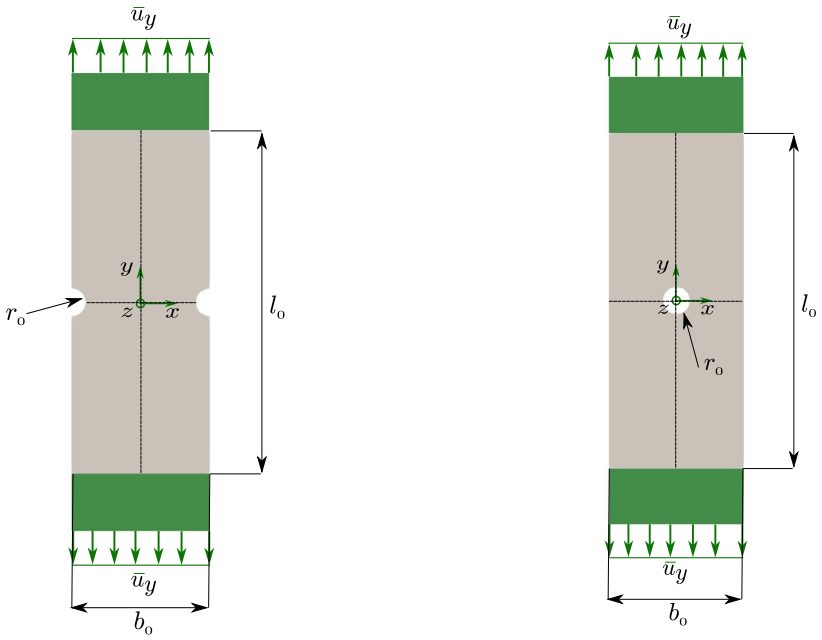

(a) Plate with lateral notches (b) Plate with central hole

Fig. 6. Specimen geometries and boundary conditions used for structural finite element simulations. Both have a length $l_0 = 50\,\text{mm}$, width $b_0 = 20\,\text{mm}$, and notch radius $r_0 = 1\,\text{mm}$, subjected to vertical displacement loading $\bar{u}_y = 5\,\text{mm}$.

Elastic parameters were extracted from the initial linear portion of the response, whereas the viscoplastic parameters were fitted to the yield point and the subsequent post-yield regime. Owing to a known model limitation — namely, that it predicts post-yield softening to begin earlier than in the experiments — certain parameters (e.g., $H_1, {}^{p}Q^{*}{}_1$) could not be estimated entirely reliably. Comparable inconsistencies have been noted in earlier publications (Parsons et al., 2004; Ognedal et al., 2012; Holopainen, 2013; Narayan and Anand, 2021). In our earlier study (Hamdoun and Mahnken, 2024a), we contrasted numerically predicted and experimentally observed strain fields using the same specimen geometry and test configuration.

The same geometry and boundary conditions are imposed in both the simulations and the experiment. The global response in Fig. 5.b shows close agreement between the measured and simulated force–displacement curves, supporting the fidelity of the modeling framework. During simulation, all arms of the biaxial specimen break at the same time, but during the experiment this is not the case, since the specimen is manually mounted and clamped in the machine, which induces many imperfections in the imposed boundary conditions.

To evaluate the behavior of the gradient-enhancement in our model, two representative geometries in Fig. 6 were investigated through finite element simulations using material parameters in Table 3. Both specimens have a rectangular shape with a length of $l_0 = 50\,\text{mm}$ and a width of $b_0 = 20\,\text{mm}$, and are subjected to uniform vertical displacements of $\bar{u}_y = 2.25\,\text{mm}$ at the top and bottom boundaries. A notch radius of $r_0 = 1\,\text{mm}$ is used in both configurations.

The first geometry, shown in Fig. 6.a, represents a plate with lateral notches, where symmetrical notches are introduced on the left and right edges to trigger stress concentrations. The second geometry, shown in Fig. 6.b, consists of a plate with a central circular hole, which serves as a stress raiser and enables the analysis of damage evolution around the hole boundary. These two configurations allow us to investigate the capability of the model to regularize damage localization and strain softening in the post-damage regime, given the same length scale l_c and the same loading $\bar{u}_y$.

Figs. 7 and 9 present the results of a mesh convergence study performed on the first specimen geometry depicted in Fig. 6.a, which consists of a plate with lateral notches. Fig. 7.a illustrates the coarse, medium, and fine mesh discretizations, while Fig. 7.b shows the corresponding reaction force–displacement curves. Here, we observe that the micromorphic regularization leads to clear mesh convergence, particularly between the medium and fine meshes. This is evident in the consistency of the peak and post-peak responses, which are typically sensitive to mesh size in conventional local damage models.

Fig. 9 further supports this observation by showing contour plots of internal field variables. Fig. 9.a displays the distribution of the local damage variable d, and Fig. 9.b shows the equivalent plastic strain e_v. Damage initiates and localizes symmetrically at the lateral notches, where stress concentration is highest. As the load increases, the damage progresses toward the center of the specimen. The plastic strain bands exhibit a similar orientation and distribution as the damage fields, reflecting the coupled nature of plasticity and damage in the constitutive model.

Both quantities exhibit mesh-independent behavior, demonstrating that the micromorphic approach effectively regularizes both variables, even though the gradient formulation is applied only to the damage variable.

In our micromorphic damage formulation, the fully coupled set of governing equations is treated in a monolithic manner and solved with a Newton–Raphson procedure. For all numerical studies considered, the nonlinear iterations were stable and exhibited nearly quadratic convergence. During damage initiation and subsequent propagation, convergence was typically achieved within about four to six Newton iterations per load increment.

Regarding discretization effort, the fine mesh required on the order of 10,000 incremental steps to complete the analysis, whereas the medium and coarse meshes converged with roughly 2000 steps. Introducing the micromorphic damage field adds an additional unknown compared with

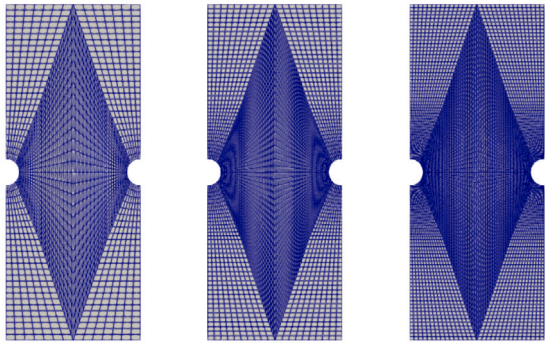

(a) Visualization of coarse, medium, and fine mesh densities

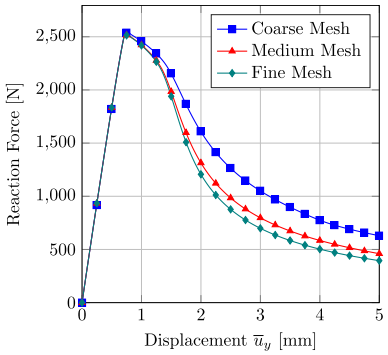

(b) Reaction force versus displacement curves illustrating the impact of micromorphic regularization

Fig. 7. Mesh convergence for the first specimen geometry in Fig. 6.a: (a) Coarse, medium, and fine meshes. (b) The micromorphic regularization enables consistent predictions across mesh resolutions, particularly in the damage-induced softening regime within medium and fine mesh densities.

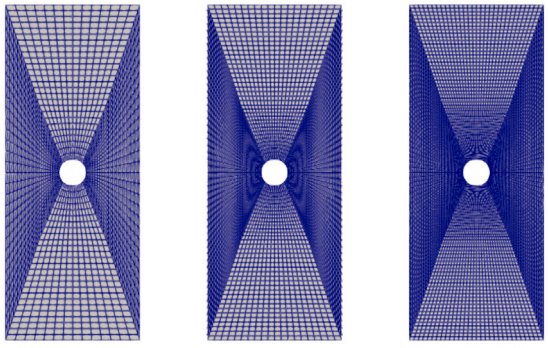

(a) Visualization of coarse, medium, and fine mesh densities

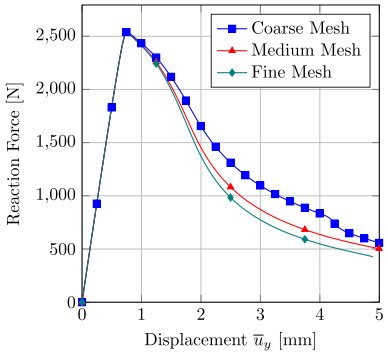

(b) Reaction force versus displacement curves illustrating the impact of micromorphic regularization

Fig. 8. Mesh convergence for the first specimen geometry in Fig. 6.b: (a) Coarse, medium, and fine meshes. (b) The micromorphic regularization enables consistent predictions across mesh resolutions, particularly in the damage-induced softening regime within medium and fine mesh densities.

a purely local viscoplastic model, thereby increasing the total number of degrees of freedom; nevertheless, the resulting computational overhead remained moderate.

To assess potential locking effects associated with nearly incompressible plastic behavior, a comparison between full integration and a selective reduced integration scheme was performed. The results showed negligible differences in both peak load and post-peak response.

All simulations presented in this work were carried out using full numerical integration. No locking artifacts or spurious stiffening were observed. The numerical response exhibits the expected plastic deformation followed by gradual softening due to damage evolution, indicating that volumetric locking does not affect the reported results.

Fig. 8 presents a mesh convergence study for a plate with a central hole, using coarse, medium, and fine mesh resolutions, as depicted in Fig. 8.a. The reaction force–displacement curves in Fig. 8.b illustrate that micromorphic regularization achieves consistent results within medium and fine meshes.

Fig. 10 provides contour plots of the local damage variable d and equivalent plastic strain e_v. Damage in Fig. 10.a initiates around the central hole, where stress concentration is highest, and progresses through the whole cross section of the specimen. The equivalent plastic strain patterns in Fig. 10.b evolve similarly. The results of both variables highlight the success of the micromorphic approach in minimizing mesh density dependence within medium and fine meshes.

5. Conclusion

We have presented a gradient-enhanced viscoplastic damage model for glassy polymers that unifies plasticity and damage within a single, thermodynamically consistent framework. Both mechanisms are formulated from energy and potential functions and evolve through Arrhenius-type multipliers. This formulation preserves thermodynamic consistency and enables consistent evolution equations and algorithmic tangents for finite element implementation.

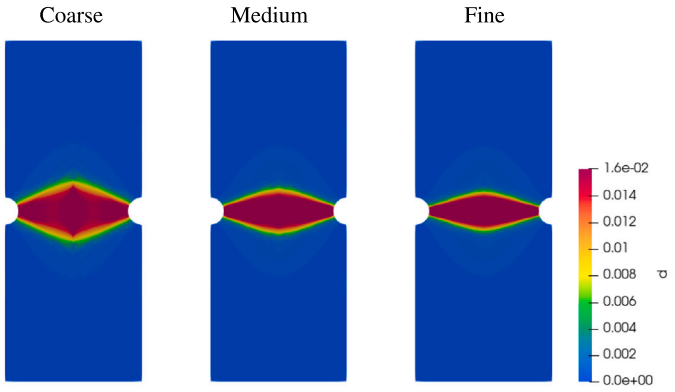

(a) Local damage variable d.

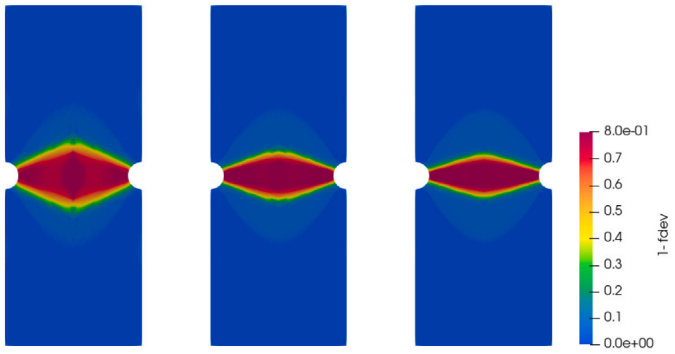

(b) Saturation of the deviatoric damage function f_{dev}.

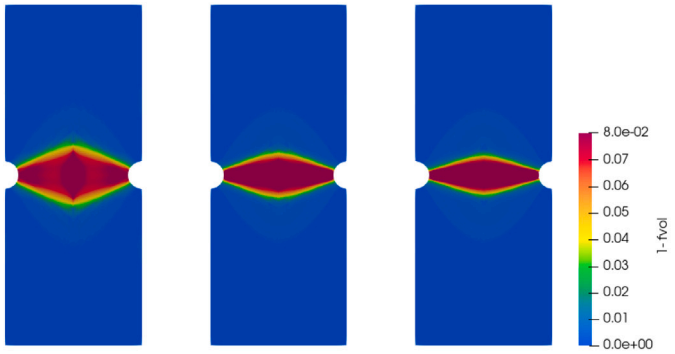

(c) Saturation of the volumetric damage function f_{vol}.

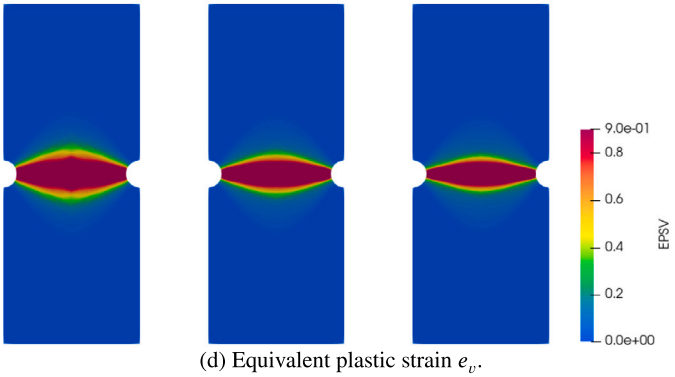

(d) Equivalent plastic strain e_v.

Fig. 9. Illustration of a structural FE-example employing the specimen geometry depicted Fig. 6.a using micromorphic regularization for the mesh densities in Fig. 7.a: (a) Distribution of the damage field d; (b–c) Visualization of the saturation behavior for the deviatoric and volumetric damage components, f_{dev}, and f_{vol}, respectively, highlighting a degradation of approximately 80% in the deviatoric contribution and 8% in the volumetric one; (d) Equivalent plastic strain field e_v. The results demonstrate strong agreement between the medium and fine mesh levels for all plotted quantities.

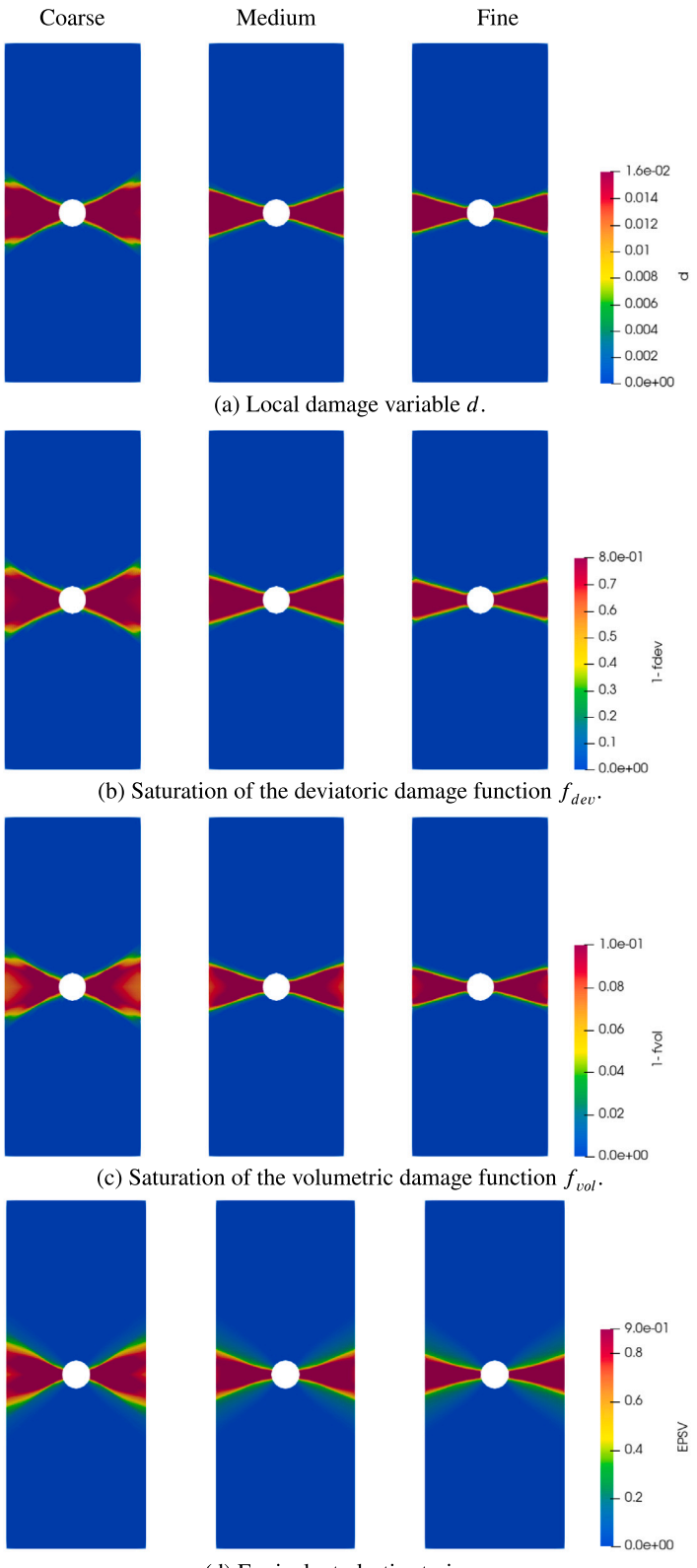

(a) Local damage variable d.

(b) Saturation of the deviatoric damage function f_{dev}.

(c) Saturation of the volumetric damage function f_{vol}.

(d) Equivalent plastic strain e_v.

Fig. 10. Illustration of a structural FE-example employing the specimen geometry depicted in Fig. 6.b with micromorphic regularization applied across the three mesh densities shown in Fig. 8.a: (a) Contour plots representing the damage variable d; (b–c) Contour plots illustrating the saturation levels of the deviatoric and volumetric damage functions, f_{dev}, and f_{vol}, respectively, indicating an 80% material degradation due to the deviatoric part and 10% due to the volumetric part; (d) Contour plots of the plastic strain e_v. The contour plots show nearly identical results for medium and fine meshes across all variables considered.

Table 3
Material parameter used for structural FE-examples.

E [MPa]	θ [K]	ν [−]	$\dot{\lambda}_0$ [s^{-1}]	A_p [K/MPa]	H_1 [MPa]
1643	293.15	0.29	0.1287	140.0	45.797
H_2 [MPa]	Q_0 [MPa]	Q_1^* [MPa]	H_{d1} [MPa]	H_{d2} [MPa]	Q_{d1}^* [MPa]
116.550	53.031	12.3	0.0	100.	12.
Q_{d01} [MPa]	Q_{d02} [MPa]	η_{dev1} [−]	η_{dev2} [−]	η_{vol1} [−]	η_{vol2} [−]
75.	75.	90.	90.	5.	5.
A_{d1} [K/MPa]	A_{d2} [K/MPa]	$\dot{\lambda}_{d01}$ [s^{-1}]	$\dot{\lambda}_{d02}$ [s^{-1}]	$\mathcal{H}$	$\mathcal{A}$
80	80	90.3	90.3	6000	900

The model captures the pronounced asymmetry between tension and compression by introducing a stress-mode weighting function, where damage activates under tensile loading while remaining suppressed in compression.

We compared the implemented model to a uniaxial tensile test on polycarbonate of simple geometry. The global force–displacement curve agrees well with the experiment, lending confidence to the constitutive structure and the numerical realization. We note, however, that the available experiment probes plasticity without measurable damage evolution. The experimental investigation of damage is still required for full validation of the theory. The micromorphic regularization is effective, where the internal length scale ensures mesh-objective responses and aligns damage and plastic-strain localization, even though the gradient acts only on damage.

Building on these results, we will design and conduct dedicated experiments across multiple specimen geometries and loading scenarios over different ranges of strain rates, with the specific goal of exciting and quantifying tensile-damage evolution. Additionally, in future work we will perform systematic parameter identification as in Mahnken and Kuhl (1999) and Mahnken (2004), with particular focus on the micromorphic parameters that govern regularization. The presented formulation and numerical evidence provide a robust foundation for this next stage.

CRediT authorship contribution statement

Ayoub Hamdoun: Writing – original draft, Visualization, Validation, Supervision, Software, Resources, Project administration, Methodology, Investigation, Formal analysis, Data curation, Conceptualization. **Rolf Mahnken:** Writing – review & editing, Supervision, Resources, Project administration, Methodology, Funding acquisition, Conceptualization. **Richard Ostwald:** Writing – review & editing, Supervision, Resources, Project administration.

Declaration of competing interest

The authors declare that they have no known competing financial interests or personal relationships that could have appeared to influence the work reported in this paper.

Acknowledgments

The authors appreciate the financial support of the project under Grant MA 1979/27-1 from Deutsche Forschungsgemeinschaft (DFG), Germany. We also appreciate financial support of the Paderborn University for the Open Access Publishing funding. The authors used ChatGPT (OpenAI) for improving grammar of the manuscript.

Appendix A. Thermodynamic consistency

For thermodynamic consistency of the material model under consideration, it is sufficient that the Clausius–Duhem inequality (19) is fulfilled. Using Eqs. ((24).1), ((24).3) and the evolution Eqs. (26), the Clausius–Duhem inequality (19) re-writes as

$$\begin{aligned} \mathcal{D}^{red} &= \mathbf{T} : \dot{\mathbf{E}}^p - \sum_{i=1}^{2} {}^pQ_i\, {}^p\dot{q}_i + Y_d \dot{d} - \sum_{i=1}^{2} {}^dQ_i\, {}^d\dot{q}_i \\ &= \dot{\lambda}_p\, {}^pQ \underbrace{\left(m_p \left(\frac{\sigma_v}{{}^pQ} \right)^{m_p} - 1 \right)}_{\geq 0} + \dot{\lambda}_p\, {}^dQ \frac{{}^pQ_1^2}{Q_1^*} + \dot{\lambda}_d \underbrace{\left(m_d \left(\frac{Y_d}{{}^dQ} \right)^{m_d} - 1 \right)}_{\geq 0} + \dot{\lambda}_d \frac{{}^dQ_1^2}{{}^dQ^*_1} \geq 0, \end{aligned} \tag{A.1}$$

since $\sigma_v / {}^pQ \gg 1$ and $Y_d / {}^dQ \gg 1$.

Appendix B. Discretization of bilinear and tangent forms

$$
\begin{aligned}
&1. \quad f_u^{\text{int }e}[\mathbf{u},\phi,\delta\mathbf{u}] &&= \langle S_{IJ}\,\delta u^e_{ai} F_{iI} N_{a,J}(\underline{\xi})\rangle_{\mathscr{B}_e} = \delta u^e_{ia} f^{in,u}_{ia}, \quad \text{where}\\
&\qquad f^{in,u}_{ia} &&= \langle S_{IJ} F_{iI} N_{a,J}(\underline{\xi})\rangle_{\mathscr{B}_e}\\
&2. \quad f_\phi^{\text{int}}[\mathbf{u},\phi;\delta\phi) &&= \langle \zeta_{iI}\delta d^e N_{a,I}(\underline{\xi}) + \hat{a}_i \delta d^e N_a(\underline{\xi})\rangle_{\mathscr{B}_e} = \delta u^e_{ia} f^{in,d}_{ia}, \quad \text{where}\\
&\qquad f^{in,d}_{ia} &&= \langle \zeta_{iI} N_{a,I}(\underline{\xi}) + \hat{a}_i N_a(\underline{\xi})\rangle_{\mathscr{B}_e}\\
&3. \quad f_u^{\text{ext}}[\mathbf{u}] &&= \langle [\boldsymbol{b}]_i \delta u^e_{ia} N_a(\underline{\xi})\rangle_{\mathscr{B}_e} + \langle [\bar{\boldsymbol{T}}]_i \delta u^e_{ia} N_a(\underline{\xi})\rangle_{\partial\mathscr{B}_e} = \delta u^e_{ia} f^{ex,u}_{ia}, \quad \text{where}\\
&\qquad f^{ex,u}_{ia} &&= \langle [\boldsymbol{b}]_i N_a(\underline{\xi})\rangle\mathscr{B}_e + \langle [\bar{\boldsymbol{T}}]_i N_a(\underline{\xi})\rangle_{\partial\mathscr{B}_e}\\
&4. \quad f_\phi^{\text{ext}}[\phi) &&= \langle [m]_i \delta d^e N_a(\underline{\xi})\rangle\mathscr{B}_e + \langle [\bar{T}_m]_i \delta u^e_{ia} N_a(\underline{\xi})\rangle_{\partial\mathscr{B}_e} = \delta d^e{}_a f^{in,d}_{ia}, \quad \text{where}\\
&\qquad f^{in,d}_{ia} &&= \langle [m]_i N_a(\underline{\xi})\rangle\mathscr{B}_e + \langle [\bar{T}_m]_i N_a(\underline{\xi})\rangle_{\partial\mathscr{B}_e}.
\end{aligned}
\tag{B.2}
$$

By use of the algorithmic tangent moduli of (46) in index notation

$$
\begin{aligned}
&1. \quad \mathbb{C}^1_{IJKL} &&= 2\frac{\partial S_{IJ}}{\partial C_{KL}}\\
&2. \quad \mathbb{C}^2_{IJ} &&= \frac{\partial S_{IJ}}{\partial d}\\
&3. \quad \mathbb{C}^{31}_{IKL} &&= 2\frac{\partial \zeta_I}{\partial C_{KL}}, \qquad \mathbb{C}^{32}_{KL} = 2\frac{\partial \hat{a}}{\partial C_{KL}}\\
&4. \quad \mathbb{C}^{41}_{IK} &&= \frac{\partial \zeta_I}{\partial H_K}, \qquad \mathbb{C}^{42} = \frac{\partial \hat{a}}{\partial d}
\end{aligned}
\tag{B.3}
$$

the tangent forms in Eqs. (45) in terms of the reference configuration for each element e are

$$
\begin{aligned}
&1. \quad D^e_{\mathbf{u}} f_u^{\text{int}}[\mathbf{u},\phi;\delta\mathbf{u}]\cdot\Delta\mathbf{u} &&= \langle \delta u^e_{ai} F_{iI} N_{a,J}(\underline{\xi}) \mathbb{C}^1_{IJKL} F_{kK} N_{b,L} \Delta u^e_{bk}\\
&\qquad &&\quad + \delta u^e_{ai} N_{a,I}(\underline{\xi}) S_{IJ} N_{b,J}(\underline{\xi}) \delta_{IJ} \Delta u^e_{bk}\rangle_{\mathscr{B}_e}\\
&\qquad &&= \delta u^e_{ai} k^{uu}_{abik} \Delta u^e_{kb}, \quad \text{where}\\
&\qquad k^{uu}_{abik} &&= \langle F_{iI} N_{a,J}(\underline{\xi}) \mathbb{C}^1_{IJKL} F_{kK} N_{b,L}(\underline{\xi}) + N_{a,I}(\underline{\xi}) S_{IJ} N_{b,J}(\underline{\xi}) \delta_{IJ}\rangle_{\mathscr{B}_e}\\
&2. \quad D^e_{\phi} f_u^{\text{int}}[\mathbf{u},\phi;\delta\mathbf{u}]\cdot\Delta\phi &&= \langle \delta u^e_{ai} F_{iI} N_{a,J}(\underline{\xi}) \mathbb{C}^2_{IJ} N_b(\underline{\xi}) \Delta d^e\rangle_{\mathscr{B}_e}\\
&\qquad &&= \delta u^e_{ai} k^{u\phi}_{abik} \Delta d^e, \quad \text{where}\\
&\qquad k^{u\phi}_{abik} &&= \langle N_{a,I}(\underline{\xi}) F_{iJ} \mathbb{C}^2_{IJ} N_b(\underline{\xi})\rangle_{\mathscr{B}_e}\\
&3. \quad D^e_{\mathbf{u}} f_\phi^{\text{int}}[\mathbf{u},\phi;\delta\phi]\cdot\Delta\mathbf{u} &&= \langle \delta d^e N_{a,I}(\underline{\xi}) \mathbb{C}^{31}_{IKL} F_{kK} N_{b,L}(\underline{\xi}) \Delta u^e_{bk} + \delta d^e N_a(\underline{\xi}) \mathbb{C}^{32}_{KL} F_{kK} N_{b,L}(\underline{\xi}) \Delta u^e_{bk}\rangle \mathscr{B}_e\\
&\qquad &&= \delta d^e k^{\phi u}_{abik} \Delta u^e_{bk}, \quad \text{where}\\
&\qquad k^{\phi u}_{abik} &&= \langle N_a(\underline{\xi}) \mathbb{C}^{32}_{KL} F_{kK} N_{b,L}(\underline{\xi})\rangle_{\mathscr{B}_e}\\
&4. \quad D^e_{\phi} f_\phi^{\text{int}}[\mathbf{u},\phi;\delta\phi]\cdot\Delta\phi &&= \langle \delta d^e N_{a,I}(\underline{\xi}) \mathbb{C}^{41}_{IK} N_{b,K} \Delta d^e + \delta d^e N_a(\underline{\xi}) \mathbb{C}^{42} N_b(\underline{\xi}) \Delta d^e\rangle_{\mathscr{B}_e}\\
&\qquad &&= \delta d^e k^{\phi\ \phi}_{abik} \Delta d^e, \quad \text{where}\\
&\qquad k^{\phi\ \phi}_{abik} &&= \langle N_{a,I}(\underline{\xi}) \mathbb{C}^{41}_{IK} N_{b,K}(\underline{\xi}) + N_a(\underline{\xi}) \mathbb{C}^{42} N_b(\underline{\xi})\rangle_{\mathscr{B}_e}.
\end{aligned}
\tag{B.4}
$$

Appendix C. Derivations of the Jacobian entries

For completeness we list the partial derivatives entering Eq. (57). Differentiating Eq. ((53).2) yields

$$
J_{11} = \frac{\partial r_p}{\partial \|\tilde{\mathbf{T}}_{dev}\|} = -1 \;-\; 2G\, f^{-1}_{dev}(d) \sqrt{\frac{3}{2}}\, m_p \left(\frac{\sigma_v}{{}^p\!Q}\right)^{m_p-1} \frac{\partial \Delta\lambda_p}{\partial \|\tilde{\mathbf{T}}_{dev}\|} \;-\; 2G\, f^{-1}_{dev}(d)\, \Delta\lambda_p \frac{m_p(m_p-1)}{{}^p\!Q} \frac{3}{2} \left(\frac{\sigma_v}{{}^p\!Q}\right)^{m_p-2},
\tag{C.5}
$$

and, using Eqs. (54) and ((24).1),

$$
J_{12} = \frac{\partial \Delta\lambda_p}{\partial \|\tilde{\mathbf{T}}_{dev}\|} = \sqrt{\frac{3}{2}}\, m_p\, \Delta\lambda_p \frac{A_p}{\theta} \left(\frac{\sigma_v}{{}^p\!Q}\right)^{m_p-1}.
\tag{C.6}
$$

The derivative with respect to d reads

$$
J_{21} = \frac{\partial r_p}{\partial d} = -2G\,\Delta\lambda_p \sqrt{\frac{3}{2}}\, m_p \left(\frac{\sigma_v}{{}^p\!Q}\right)^{m_p-1} \frac{\partial f^{-1}_{dev}(d)}{\partial d},
\tag{C.7}
$$

with (cf. Eq. ((15).2))

$$
J_{22} = \frac{\partial f^{-1}_{dev}(d)}{\partial d} = \frac{\eta_{dev}(\epsilon+1)\exp(-\eta_{dev} d)}{\left(\exp(-\eta_{dev} d) + \epsilon\right)^2}.
\tag{C.8}
$$

For the damage residual r_d in Eq. ((53).3), the derivative with respect to $\|\tilde{\mathbf{T}}_{dev}\|$ gives

$$\frac{\partial r_d}{\partial \|\tilde{\mathbf{T}}_{dev}\|} = \underbrace{\frac{\partial r_d}{\partial \|\tilde{\mathbf{T}}_{dev}\|}}_{=0} + \frac{\partial r_d}{\partial \Delta\lambda_d}\frac{\partial \Delta\lambda_d}{\partial Y_d}\frac{\partial Y_d}{\partial \|\tilde{\mathbf{T}}_{dev}\|} + \frac{\partial r_d}{\partial Y_d}\frac{\partial Y_d}{\partial \|\tilde{\mathbf{T}}_{dev}\|}, \tag{C.9}$$

where

$$\frac{\partial r_d}{\partial \Delta\lambda_d} = -\,m_d\left(\frac{Y_d}{{}^dQ}\right)^{m_d-1}, \qquad \frac{\partial \Delta\lambda_d}{\partial Y_d} = \Delta\lambda_d\,\frac{A_d m_d}{\theta}\left(\frac{Y_d}{{}^dQ}\right)^{m_d-1}, \tag{C.10}$$

and from Eq. (55),

$$\frac{\partial Y_d}{\partial \|\tilde{\mathbf{T}}_{dev}\|} = -\,f'_{dev}(d)\,\frac{\|\tilde{\mathbf{T}}_{dev}\|}{2G}, \tag{C.11}$$

and derivation with respect to Y_d yields

$$\frac{\partial r_d}{\partial Y_d} = -\,\Delta\lambda_d\,\frac{m_d(m_d-1)}{{}^dQ}\left(\frac{Y_d}{{}^dQ}\right)^{m_d-2}. \tag{C.12}$$

Finally, the derivation of r_d with respect to d gives

$$\frac{\partial r_d}{\partial d} = \underbrace{\frac{\partial r_d}{\partial d}}_{=1} + \frac{\partial r_d}{\partial \Delta\lambda_d}\frac{\partial \Delta\lambda_d}{\partial Y_d}\frac{\partial Y_d}{\partial d} + \frac{\partial r_d}{\partial Y_d}\frac{\partial Y_d}{\partial d}, \tag{C.13}$$

with

$$\begin{aligned} &1.\ \frac{\partial Y_d}{\partial d} = -\,f''_{dev}(d)\,G\left(\frac{\|\tilde{\mathbf{T}}_{dev}\|}{2G}\right)^2 - f''_{vol}(d)\,\frac{K}{2}\left(\mathrm{tr}\left[\mathbf{E}^e\right]\right)^2 - {}^tH, \\ &2.\ f''_{dev}(d) = \frac{\eta_{dev}^2\exp(-\eta_{dev}d)}{1+\epsilon}, \qquad 3.\ f''_{vol}(d) = \eta_{vol}^2\,f_{vol}(d). \end{aligned} \tag{C.14}$$

Appendix D. Derivations of local unknowns with respect to global unknowns

The sensitivities of the local variables $\underline{x} = [\|\tilde{\mathbf{T}}_{dev}\|; d]$ with respect to the global variables $\underline{X} = [\mathbf{E}; \phi]$ are obtained from the local problem (53) via the implicit function theorem

$$\boldsymbol{r}[\underline{x}, \underline{x}(\underline{X})] = 0 \Rightarrow \frac{\mathrm{d}\boldsymbol{r}}{\mathrm{d}\underline{X}} = \frac{\partial \boldsymbol{r}}{\partial \underline{X}} + \frac{\partial \boldsymbol{r}}{\partial \underline{x}}\frac{\mathrm{d}\underline{x}}{\mathrm{d}\underline{X}} = 0 \Rightarrow \frac{\mathrm{d}\underline{x}}{\mathrm{d}\underline{X}} = -\,\boldsymbol{J}^{-1}\,\frac{\partial \boldsymbol{r}}{\partial \underline{X}}, \text{ where } \frac{\partial \boldsymbol{r}}{\partial \underline{X}} = \begin{bmatrix} \dfrac{\partial r_p}{\partial \mathbf{E}} & \dfrac{\partial r_p}{\partial \phi} \\ \dfrac{\partial r_d}{\partial \mathbf{E}} & \dfrac{\partial r_d}{\partial \phi} \end{bmatrix}. \tag{D.15}$$

The derivative of residual vector $\boldsymbol{r}$ with respect of $\mathbf{E}$ is

$$\begin{aligned} &1.\ \frac{\partial r_p}{\partial \mathbf{E}} = \frac{\partial \|\mathbf{T}^{tr}_{dev}\|}{d\mathbf{E}} = 2\,G\,\mathbf{N}, \\ &2.\ \frac{\partial r_d}{\partial \mathbf{E}} = \frac{\partial r_d}{\partial \Delta\lambda_d}\frac{\partial \Delta\lambda_d}{\partial Y_d}\frac{\partial Y_d}{\partial \mathbf{E}} + \frac{\partial r_d}{\partial Y_d}\frac{\partial Y_d}{\partial \mathbf{E}}, \quad \text{where} \\ &3.\ \frac{\partial Y_d}{\partial \mathbf{E}} = -\,f'_{vol}(d)\,K\,\mathrm{tr}\left[\mathbf{E}^e\right]\,\mathbf{1}, \end{aligned} \tag{D.16}$$

and the derivative of residual vector $\boldsymbol{r}$ with respect of ϕ is

$$\begin{aligned} &1.\ \frac{\partial r_p}{\partial \phi} = 0, \\ &2.\ \frac{\partial r_d}{\partial \phi} = \frac{\partial r_d}{\partial \Delta\lambda_d}\frac{\partial \Delta\lambda_d}{\partial Y_d}\frac{\partial Y_d}{\partial \phi} + \frac{\partial r_d}{\partial Y_d}\frac{\partial Y_d}{\partial \phi}, \quad \text{where} \quad \frac{\partial Y_d}{\partial \phi} = {}^tH. \end{aligned} \tag{D.17}$$

Appendix E. Algorithmic tangent moduli $\mathbb{C}^1$

Invoking the constitutive relation between the Second Piola–Kirchhoff stress $\mathbf{S}$ and the Hill stress $\mathbf{T}$ in Eq. ((18).2), the algorithmic tangent modulus in Eq. ((46).1) follows by formal application of the chain rule (see Miehe and Lambrecht, 2000):

$$\begin{aligned} &1.\ \mathbb{C}^1 = 2\frac{\partial \mathbf{S}}{\partial \mathbf{C}} = \mathbb{P} : \mathbb{H} : \mathbb{P} + \mathbf{T} : \mathbb{L}, \quad \text{where} \\ &2.\ \mathbb{H} = \frac{\partial \mathbf{T}}{\partial \mathbf{E}}, \qquad 3.\ \mathbb{L} = 4\frac{\partial^2 \mathbf{E}}{\partial \mathbf{C}\otimes\partial \mathbf{C}}. \end{aligned} \tag{E.18}$$

Here, in addition to the projection tensor $\mathbb{P}$ defined in Eq. ((4).2), we introduced the sixth-order tensor $\mathbb{L}$ and the material modulus $\mathbb{H}$. The latter is obtained by differentiating the Hill stress $\mathbf{T}$ with respect to the total strain tensor $\mathbf{E}$ under its standard volumetric–deviatoric split. The full expressions of $\mathbb{H}$ and all intermediate sensitivities are collected in Appendix I.

Appendix F. Algorithmic tangent modulus $\mathbb{C}^2$

The algorithmic tangent modulus $\mathbb{C}^2$ defined in (46).2 follows, by a direct chain rule argument, as

$$\mathbb{C}^2 = \frac{\partial \mathbf{S}}{\partial \phi} = \left(\frac{\partial \mathbf{T}}{\partial \|\tilde{\mathbf{T}}_{dev}\|} \frac{\partial \|\tilde{\mathbf{T}}_{dev}\|}{\partial \phi} + \frac{\partial \mathbf{T}}{\partial d} \frac{\partial d}{\partial \phi} \right) : \mathbb{P}. \tag{F.19}$$

The sensitivities of the internal variables with respect to ϕ are obtained from Eq. (D.15) via the implicit-function theorem. All remaining elementary partial derivatives and driving-force terms are deferred to the Appendix for compactness.

Appendix G. Algorithmic tangent moduli $\mathbb{C}^{31}$ and $\mathbb{C}^{32}$

The algorithmic tangent modulus $\mathbb{C}^{31}$, as defined in Eq. ((46).3), is given by

$$\mathbb{C}^{31} = 2\frac{\partial \boldsymbol{\zeta}}{\partial \mathbf{C}} = \mathbf{0}. \tag{G.20}$$

Taking the derivative of the microforce in Eq. ((16).3), we obtain

$$\mathbb{C}^{32} = 2\frac{\partial \hat{a}}{\partial \mathbf{C}} = 2\frac{\partial {}^{\chi}H(\phi - d)}{\partial \mathbf{C}} = -2\,{}^{\chi}H \frac{\partial d}{\partial \mathbf{C}} = -2\,{}^{\chi}H \frac{\partial d}{\partial \mathbf{E}} : \frac{\partial \mathbf{E}}{\partial \mathbf{C}} = -{}^{\chi}H \frac{\partial d}{\partial \mathbf{E}} : \mathbb{P}, \tag{G.21}$$

where the derivative $\frac{\partial d}{\partial \mathbf{E}}$ is obtained from Eq. (D.15).

Appendix H. Algorithmic tangent moduli $\mathbb{C}^{41}$ and $\mathbb{C}^{42}$

By differentiating the microstress in Eq. ((16).4), the algorithmic tangent modulus $\mathbb{C}^{41}$ in Eq. ((46).3) is obtained as

$$\mathbb{C}^{41} = \frac{\partial \boldsymbol{\zeta}}{\partial \boldsymbol{H}} = \frac{\partial {}^{\chi}A\ \boldsymbol{H}}{\partial \boldsymbol{H}} = {}^{\chi}A\mathbf{1} \tag{H.22}$$

where $\mathbf{1}$ is a second order unit tensor. Similarly, differentiating the microforce in Eq. ((16).3) gives the algorithmic tangent modulus $\mathbb{C}^{42}$ in Eq. ((46).3)

$$\mathbb{C}^{42} = \frac{\partial \hat{a}}{\partial \phi} = \frac{\partial {}^{\chi}H(\phi - d)}{\partial \phi} = {}^{\chi}H(1 - \frac{\partial d}{\partial \phi}), \tag{H.23}$$

The derivative $\frac{\partial d}{\partial \phi}$ is in Eq. (D.15).

Appendix I. Details for $\mathbb{H}$ and auxiliary derivatives

The decomposition of $\mathbb{H}$ consistent with the volumetric–deviatoric split reads

$$\begin{aligned}
&1.\quad \mathbb{H} = \frac{\partial \mathbf{T}_{vol}}{\partial \mathbf{E}} + \frac{\partial \mathbf{T}_{dev}}{\partial \mathbf{E}}, \quad \text{where}\\
&2.\quad \frac{\partial \mathbf{T}_{vol}}{\partial \mathbf{E}} = f_{vol}(d)\, K\, \mathbf{1} \otimes \mathbf{1} + K\,\mathrm{tr}(\mathbf{E}^e)\,\mathbf{1} \otimes \frac{\partial f_{vol}(d)}{\partial \mathbf{E}},\\
&3.\quad \frac{\partial \mathbf{T}_{dev}}{\partial \mathbf{E}} = f_{dev}(d) \frac{\partial \mathbf{T}^{tr}_{dev}}{\partial \mathbf{E}} + \mathbf{T}^{tr}_{dev} \otimes \frac{\partial f_{dev}(d)}{\partial \mathbf{E}} - 2\,G\sqrt{\frac{3}{2}}\, m_p \frac{\partial \left(\Delta\lambda_p \left(\frac{\sigma_v}{{}^{p}Q}\right)^{m_p - 1} \mathbf{N} \right)}{\partial \mathbf{E}}.
\end{aligned} \tag{I.24}$$

The elementary derivatives used in (I.24) are

$$\frac{\partial \mathbf{T}^{tr}_{dev}}{\partial \mathbf{E}} = 2\,G\,\mathbb{I}^{dev}, \tag{I.25}$$

and

$$\frac{\partial}{\partial \mathbf{E}} \left(\Delta\lambda_p \left(\frac{\sigma_v}{{}^{p}Q}\right)^{m_p - 1} \mathbf{N} \right) = \left(\frac{\sigma_v}{{}^{p}Q}\right)^{m_p - 1} \mathbf{N} \otimes \frac{\partial \Delta\lambda_p}{\partial \mathbf{E}} + \Delta\lambda_p \mathbf{N} \otimes \frac{\partial}{\partial \mathbf{E}} \left(\frac{\sigma_v}{{}^{p}Q}\right)^{m_p - 1} + \Delta\lambda_p \left(\frac{\sigma_v}{{}^{p}Q}\right)^{m_p - 1} \frac{\partial \mathbf{N}}{\partial \mathbf{E}}. \tag{I.26}$$

For the factors in (I.26) we use

$$\begin{aligned}
&1.\quad \frac{\partial \Delta\lambda_p}{\partial \mathbf{E}} = \frac{\partial \Delta\lambda_p}{\partial \|\tilde{\mathbf{T}}_{dev}\|} \frac{\partial \|\tilde{\mathbf{T}}_{dev}\|}{\partial \mathbf{E}}, \quad \text{where}\\
&2.\quad \frac{\partial \Delta\lambda_p}{\partial \|\tilde{\mathbf{T}}_{dev}\|} = \sqrt{\frac{3}{2}}\, m_p\, \Delta\lambda_p \frac{A}{\theta} \left(\frac{\sigma_v}{{}^{p}Q}\right)^{m_p - 1},
\end{aligned} \tag{I.27}$$

and

$$\frac{\partial}{\partial \mathbf{E}} \left(\frac{\sigma_v}{{}^{p}Q}\right)^{m_p - 1} = \frac{(m_p - 1)}{{}^{p}Q} \sqrt{\frac{3}{2}} \left(\frac{\sigma_v}{{}^{p}Q}\right)^{m_p - 2} \frac{\partial \|\tilde{\mathbf{T}}_{dev}\|}{\partial \mathbf{E}}. \tag{I.28}$$

The flow direction sensitivity is

$$\frac{\partial \mathbf{N}}{\partial \mathbf{E}} = \frac{2\,G}{\|\mathbf{T}^{tr}_{dev}\|} \left(\mathbb{I}^{dev} - \mathbf{N} \otimes \mathbf{N} \right). \tag{I.29}$$

The derivatives of the degradation functions with respect to $\mathbf{E}$ (via d) are

$$\begin{aligned}
&1.\quad \frac{\partial f_{vol}(d)}{\partial \mathbf{E}} = -\frac{\eta_{dev} \exp(-\eta_{dev} d)}{1 + \epsilon} \frac{\partial d}{\partial \mathbf{E}},\\
&2.\quad \frac{\partial f_{dev}(d)}{\partial \mathbf{E}} = -\eta_{dev}\, f_{dev}(d) \frac{\partial d}{\partial \mathbf{E}}.
\end{aligned} \tag{I.30}$$

Appendix J. Details for $\mathbb{C}^2$ auxiliary derivatives

The Hill-stress sensitivities used in (F.19) read

$$\begin{aligned} 1.\quad \frac{\partial \mathbf{T}}{\partial \|\tilde{\mathbf{T}}_{dev}\|} &= -2G\, m_p \sqrt{\frac{3}{2}}\, \mathbf{N} \left[\frac{\partial \Delta\lambda_p}{\partial \|\tilde{\mathbf{T}}_{dev}\|} \left(\frac{\sigma_v}{{}^pQ}\right)^{m_p-1} + \Delta\lambda_p \frac{(m_p-1)}{{}^pQ} \sqrt{\frac{3}{2}} \left(\frac{\sigma_v}{{}^pQ}\right)^{m_p-2} \right], \\ 2.\quad \frac{\partial \mathbf{T}}{\partial d} &= f'_{vol}(d)\, K\, \mathrm{tr}(\mathbf{E}^e)\, \mathbf{1} + f'_{dev}(d)\, \mathbf{T}^{tr}_{dev}. \end{aligned} \tag{J.31}$$

Eqs. (D.17)–(J.31), together with the previously defined Jacobian J, fully specify the quantities in (F.19).

Data availability

Data will be made available on request.

References

Alves, J.L., Ferreira, B.P., Andrade Pires, F.M., 2023. A constitutive model for amorphous thermoplastics from low to high strain rates: Formulation and computational aspects. Int. J. Plast. 169, 103712.

Anand, L., Gurtin, M.E., 2003. A theory of amorphous solids undergoing large deformations, with application to polymeric glasses. Int. J. Solids Struct. 40 (6), 1465–1487.

Argon, A., 1973. A theory for the low-temperature plastic deformation of glassy polymers. Phil. Mag. 28 (4), 839–865.

Boyce, M.C., Parks, D.M., Argon, A.S., 1988. Large inelastic deformation of glassy polymers. part I: rate dependent constitutive model. Mech. Mater. 7 (1), 15–33.

Brepols, T., Wulfinghoff, S., Reese, S., 2017a. A gradient-enhanced two-surface damage-plasticity model. Comput. Methods Appl. Mech. Engrg. 318, 349–381.

Brepols, T., Wulfinghoff, S., Reese, S., 2017b. Gradient-extended two-surface damage-plasticity: Micromorphic formulation and numerical aspects. Int. J. Plast. 97, 64–106.

Comi, C., 2001. A non-local model with tension and compression damage mechanisms. Eur. J. Mech. A Solids 20, 1–22.

de Borst, R., Pamin, J., 1996. Some novel developments in finite element procedures for gradient-dependent plasticity. Internat. J. Numer. Methods Engrg. 39, 2477–2505.

Engelen, R.A.B., Geers, M.G.D., de Borst, R., 2006. Gradient-enhanced damage plasticity: formulation and computational aspects. Internat. J. Numer. Methods Engrg. 67, 1122–1148.

Estevez, R., Van der Giessen, E., 2005. Modeling and computational analysis of fracture of glassy polymers. In: Intrinsic Molecular Mobility and Toughness of Polymers II. Springer, pp. 195–234.

Ferreira, B.P., Alves, J.L., Andrade Pires, F.M., 2023. An efficient finite strain constitutive model for amorphous thermoplastics: Fully implicit computational implementation and optimization-based parameter calibration. Comput. Struct. 281, 107007.

Forest, S., 1998. Continuum thermomechanics of nonlinear micromorphic, strain and stress gradient media. Phil. Trans. R. Soc. A 356, 2235–2265.

Forest, S., 2009. Micromorphic approach for gradient elasticity, viscoplasticity, and damage. J. Eng. Mech. 135, 117–131.

Forest, S., Cordero, N.M., Busso, E.P., 2011. First and second gradient elasticity of crystalline materials. J. Mech. Phys. Solids 59, 458–472.

Friedlein, J., Mergheim, J., Steinmann, P., 2023. Efficient gradient enhancements for plasticity with ductile damage in the logarithmic strain space. Eur. J. Mech. A Solids 99, 104946.

Geers, M.G.D., de Borst, R., Peerlings, R.H.J., 1998. Damage and crack modeling in single-edge and double-edge notched concrete beams. Eng. Fract. Mech. 65, 219–247.

GOM, A., Manual, U., 2011. The basics of strain. In: GOM–Gesellschaft Für Optische Messtechnik. Braunschweig, Germany.

Hamdoun, A., Mahnken, R., 2024a. A large deformation gradient theory for glassy polymers by means of micromorphic regularization. Arch. Appl. Mech. 94 (5), 1221–1242.

Hamdoun, A., Mahnken, R., 2024b. Uniaxial and biaxial experimental investigation of glassy polymers. Polymer 299, 126981.

Hencky, H., 1928. Über die form des elastizitätsgesetzes bei ideal elastischen stoffen. Z. Tech. Phys. 9, 215–220.

Holopainen, S., 2013. Modeling of the mechanical behavior of amorphous glassy polymers under variable loadings and comparison with state-of-the-art model predictions. Mech. Mater. 66.

Holthusen, L., Mergheim, J., Steinmann, P., 2022. Gradient-enhanced finite plasticity with anisotropic damage in logarithmic strain space. J. Mech. Phys. Solids 166, 104833.

Kiefer, B., Waffenschmidt, T., Sprave, L., Menzel, A., 2018. A gradient-enhanced damage model coupled to plasticity—multi-surface formulation and algorithmic concepts. Int. J. Damage Mech. 27 (2), 253–295.

Krairi, A., Doghri, I., 2014. A thermodynamically-based constitutive model for thermoplastic polymers coupling viscoelasticity, viscoplasticity and ductile damage. Int. J. Plast. 60, 163–181.

Lamm, L., Awad, A., Pfeifer, J., Holthusen, H., Felder, S., Reese, S., Brepols, T., 2024a. A gradient-extended thermomechanical model for rate-dependent damage and failure within rubberlike polymeric materials at finite strains. Int. J. Plast. 173, 103883.

Lamm, L., Pfeifer, J.M., Holthusen, H., Schaaf, B., Seewald, R., Schiebahn, A., Brepols, T., Feldmann, M., Reisgen, U., Reese, S., 2024b. Gradient-extended damage modelling for polymeric materials at finite strains: Rate-dependent damage evolution combined with viscoelasticity. Eur. J. Mech. A Solids 103, 105121.

Laschütza, P., Seelig, T., 2025. Analysis of mode I crack propagation in glassy polymers under cyclic loading. J. Mech. Phys. Solids 191, 105901.

Lemaitre, J., 1985. Coupled elasto-plasticity and damage constitutive equations. Comput. Methods Appl. Mech. Engrg. 51 (1–3), 31–49.

Mahnken, R., 2003. Creep simulation of asymmetric effects by use of stress mode dependent weighting functions. Int. J. Solids Struct. 40 (22), 6189–6209.

Mahnken, R., 2004. Identification of material parameters for constitutive equations. Encycl. Comput. Mech..

Mahnken, R., Dammann, C., 2014. Simulation of strain-induced anisotropy for polymers with weighting functions. Arch. Appl. Mech. 84, 21–41.

Mahnken, R., Kuhl, E., 1999. Parameter identification of gradient enhanced damage models with the finite element method. Eur. J. Mech. A Solids 18 (5), 819–835.

Mahnken, R., Shaban, A., 2013. Finite elasto-viscoplastic modeling of polymers including asymmetric effects. Arch. Appl. Mech. 83.

Mahnken, R., Shaban, A., Potente, H., Wilke, L., 2008. Thermoviscoplastic modelling of asymmetric effects for polymers at large strains. Int. J. Solids Struct. 45 (17), 4615–4628.

Marsden, J., Hughes, T.J.R., 1994. Mathematical Foundations of Elasticity. Dover Publications, Inc, New York.

Miehe, C., Lambrecht, M., 2000. Algorithms for computation of stresses and elasticity moduli in terms of Seth-Hill's family of generalised strain tensors. Comm. Num. Meth. Eng. 48, 323–365.

Narayan, S., Anand, L., 2021. Fracture of amorphous polymers: A gradient-damage theory. J. Mech. Phys. Solids 146, 104198.

Nguyen, V.-D., Lani, F., Pardoen, T., Morelle, X.P., Noels, L., 2016. A large strain hyperelastic viscoelastic-viscoplastic-damage constitutive model based on a multi-mechanism non-local damage continuum for amorphous glassy polymers. Int. J. Solids Struct. 96, 192–216.

Nguyen, V.-D., Noels, L., Pardoen, T., 2014. A non-local damage continuum for amorphous glassy polymers. Int. J. Solids Struct. 51, 417–431.

Ogden, R., 1984. Non-Linear Elastic Deformations. Ellis Horwood, Chichester, New York.

Ognedal, A.S., Clausen, A.H., Polanco-Loria, M., Benallal, A., Raka, B., Hopperstad, O.S., 2012. Experimental and numerical study on the behaviour of PVC and HDPE in biaxial tension. Mech. Mater. 54, 18–31.

Parsons, E., Boyce, M.C., Parks, D.M., 2004. An experimental investigation of the large-strain tensile behavior of neat and rubber-toughened polycarbonate. Polymer 45 (8), 2665–2684.

Peerlings, R.H.J., de Borst, R., Brekelmans, W.A.M., Geers, M.G.D., 1996. Gradient-enhanced damage modelling of concrete fracture. Mech. Cohesive Frict. Mater. 1, 319–342.

Peerlings, R.H.J., Geers, M.G.D., de Borst, R., Brekelmans, W.A.M., 2001. A critical comparison of nonlocal and gradient-enhanced softening continua. Int. J. Solids Struct. 38, 7723–7746.

Satouri, S., Chatzigeorgiou, G., Benaarbia, A., Meraghni, F., 2022. A gradient enhanced constitutive framework for the investigation of ductile damage localization within semicrystalline polymers. Int. J. Damage Mech. 32, 1–37.

Satouri, S., Chatzigeorgiou, G., Meraghni, F., Robert, G., 2025. Viscoelastic–viscoplastic model with ductile damage accounting for tension–compression asymmetry and hydrostatic pressure effect for polyamide 66. Eur. J. Mech. A Solids 110, 105491.
Schulte, R., Ostwald, R., Menzel, A., 2020. Gradient-enhanced modelling of damage for rate-dependent material behaviour—a parameter identification framework. Materials 13 (14), 3156.
Seth, B., 1964. Generalized strain measure with application to physical problems. In: Reiner, M., Abir, D. (Eds.), Second Order Effects in Elasticity, Plasticity and Fluid Dynamics. Pergamon Press, Oxford, Madison, pp. 162–172.
Shaban, A., Mahnken, R., Wilke, L., Potente, H., Ridder, H., 2007. Simulation of rate dependent plasticity for polymers with asymmetric effects. Int. J. Solids Struct. 44 (18), 6148–6162.
Silhavy, M., 1997. The Mechanics and Thermodynamics of Continuous Media. Springer–Verlag, Berlin.
Simo, J.C., Hughes, T.J., 2006. Computational Inelasticity, vol. 7, Springer Science & Business Media, New York.
Sprave, L., Menzel, A., 2020. A large strain gradient-enhanced ductile damage model. Int. J. Plast. 128, 102657.
Voyiadjis, G.Z., Shojaei, A., Li, G., 2012. A generalized coupled viscoplastic–viscodamage–viscohealing theory for glassy polymers. Int. J. Plast. 28, 21–45.
Wiersma, J., Sain, T., 2023. A coupled viscoplastic-damage constitutive model for semicrystalline polymers. Mech. Mater. 176, 104527.
Yin, B., Kaliske, M., 2020. A ductile phase-field model based on degrading the fracture toughness: Theory and implementation at small strain. Comput. Methods Appl. Mech. Engrg. 366, 113068.
Zaïri, F., Naït-Abdelaziz, M., Gloaguen, J., Lefebvre, J., 2008. Modelling of the elasto-viscoplastic damage behaviour of glassy polymers. Int. J. Plast. 24 (6), 945–965.
Zhao, Y., Jain, A., Müller-Plathe, F., Steinmann, P., Pfaller, S., 2024a. Investigating fracture mechanisms in glassy polymers using coupled particle–Continuum simulations. J. Mech. Phys. Solids 193, 105884.
Zhao, Y., Pfaller, S., Steinmann, P., 2024b. Multiscale modeling of fracture in glassy polymers. Eng. Fract. Mech. 301, 109845.
Zhou, Y., Qiu, Y., Peng, X., Lai, W., 2023. Modeling the viscoelastic–viscoplastic behavior of glassy polymer membranes with consideration of non-uniform sub-chains. Int. J. Solids Struct. 276, 112469.